

The importance of warm, AGN-driven outflows in the nuclear regions of nearby ULIRGs

J. Rodríguez Zaurín,^{1,2★} C. N. Tadhunter,³ M. Rose³ and J. Holt⁴

¹*Instituto de Astrofísica de Canarias, E-38205 La Laguna, Tenerife, Spain*

²*Departamento de Astrofísica, Universidad de La Laguna, E-38206 La Laguna, Tenerife, Spain*

³*Department of physics and Astronomy, University of Sheffield, Sheffield S3 7RH, UK*

⁴*Leiden Observatory, Leiden University, PO Box 9513, 2300 RA Leiden, the Netherlands*

Accepted 2013 March 6. Received 2013 March 5; in original form 2012 October 1

ABSTRACT

We present an optical spectroscopic study of a 90 per cent complete sample of nearby ULIRGs ($z < 0.175$) with optical Seyfert nuclei, with the aim of investigating the nature of the near-nuclear ($r \lesssim 3.5$ kpc) warm gas outflows. A high proportion (94 per cent) of our sample show disturbed emission line kinematics in the form of broad (FWHM > 500 km s⁻¹) and/or strongly blueshifted ($\Delta V < -150$ km s⁻¹) emission line components. This proportion is significantly higher than found in a comparison sample of nearby ultraluminous infrared galaxies (ULIRGs) that lack optical Seyfert nuclei (19 per cent). We also find evidence that the emission line kinematics of the Sy-ULIRGs are more highly disturbed than those of samples of non-ULIRG Seyferts and Palomar–Green quasars in the sense that, on average, their [O III] $\lambda\lambda 5007, 4959$ emission lines are broader and more asymmetric.

The Sy-ULIRG sample encompasses a wide diversity of emission line profiles. In most individual objects, we are able to fit the profiles of all the emission lines of different ionization with a kinematic model derived from the strong [O III] $\lambda\lambda 4959, 5007$ lines, using between two and five Gaussian components. From these fits, we derive diagnostic line ratios that are used to investigate the ionization mechanisms for the different kinematic components. We show that, in general, the line ratios are consistent with gas of supersolar abundance photoionized by a combination of AGN and starburst activity, with an increasing contribution from the AGN with increasing FWHM of the individual kinematic components, and the AGN contribution dominating for the broadest components. However, shock ionization cannot be ruled out in some cases. Our derived upper limits on the mass outflows rates and kinetic powers of the emission line outflows show that they can be as energetically significant as the neutral and molecular outflows in ULIRGs – consistent with the requirements of the hydrodynamic simulations that include AGN feedback. However, the uncertainties are large, and more accurate estimates of the radii, densities and reddening of the outflows are required to put these results on a firmer footing.

Key words: ISM: jets and outflows – ISM: kinematics and dynamics – galaxies: active – galaxies: evolution – galaxies: interactions – galaxies: Seyfert.

1 INTRODUCTION

AGN-induced outflows are increasingly recognized as a key element in the overall galaxy formation process, regulating the correlations between black hole mass and host galaxy properties (Silk & Rees 1998; Fabian 1999), and influencing the luminosity functions of galaxies, particularly at the high-luminosity end (Benson et al. 2003). Indeed, AGN feedback is now routinely incorporated

into numerical simulations of the hierarchical growth of galaxies through major galaxy mergers (Springel, Di Matteo & Hernquist 2005; Johansson, Burkert & Naab 2009). However, there remain considerable uncertainties about the exact nature of the symbiosis between black holes and their host galaxies. Consequently, the importance of AGN-induced outflows relative to those driven by the supernovae associated with the merger-induced starbursts has yet to be established observationally.

In order to test the models, it is important to identify samples of actively evolving galaxies in which both the black holes and the galaxy bulges are growing rapidly. Although much

★E-mail: javierr@iac.es

attention has been paid recently to sub-mm galaxies at high redshifts that frequently show signs of AGN activity in X-ray observations (Alexander et al. 2005, 2010; Harrison et al. 2012), there is a limit to what can be learnt in detail about the co-evolution of black holes and galaxy bulges in such objects because of their faintness. Moreover, for high-redshift galaxies many important diagnostic emission lines are shifted out of the optical/near-IR, and their outflows are difficult to resolve spatially.

Fortunately, the hierarchical evolution of galaxies is also continuing in the local Universe, albeit at a reduced rate. The ultraluminous infrared galaxies (ULIRGs: $L_{\text{IR}} > 10^{12} L_{\odot}$) represent a class of objects at relatively low redshifts in which the prodigious far-IR radiation represents the dust re-processed light of major starbursts and/or AGN buried in the nuclei of the galaxies (Sanders & Mirabel 1996). ULIRGs almost invariably show morphological evidence (e.g. tidal tails, double nuclei) consistent with triggering of the activity in major galaxy mergers (e.g. Sanders et al. 1988a; Surace et al. 1998; Surace, Sanders & Evans 2000; Surace & Sanders 2000; Kim, Veilleux & Sanders 2002; Veilleux, Kim & Sanders 2002). Based on their mid- to far-IR colours they can be sub-divided into ‘warm’ ($f_{25\ \mu\text{m}}/f_{60\ \mu\text{m}} > 0.20$) and ‘cool’ ($f_{25\ \mu\text{m}}/f_{60\ \mu\text{m}} < 0.20$) sub-types, with the warm sub-type frequently associated with visible Seyfert or quasar nuclei (e.g. Surace & Sanders 1999). In terms of evolutionary scenarios, it has been proposed that cool, starburst-dominated ULIRGs evolve into warm, AGN-dominated ULIRGs as the circumnuclear dust is dispersed by starburst- and AGN-induced outflows (Sanders et al. 1988b; Surace et al. 1998). Such scenarios are broadly consistent with current simulations of major, gas-rich galaxy mergers (Hopkins et al. 2005). Therefore, the ULIRGs represent local analogues of the rapidly evolving galaxies now being detected in large numbers in the distant Universe, but they have the considerable advantage over the high-redshift objects that they are close enough to study in detail. In this sense, the nearby ULIRGs are key objects for understanding the detailed physical mechanisms – particularly the outflows – involved in the co-evolution of supermassive black holes and their host galaxies.

As the most rapidly evolving galaxies in the local Universe, ULIRGs represent just the situation modelled in many of the most recent hydrodynamic simulations of gas-rich mergers (e.g. di Matteo, Springel & Hernquist 2005; Johansson et al. 2009). In the final stages of such mergers, as the nuclei coalesce, the simulations predict that the supermassive black holes accrete at sufficiently high rates to produce luminous, quasar-like AGN; the outflows associated with the AGN are potentially capable of ejecting the remaining gas and halting star formation in the bulges of the merger remnants. However, fine-tuning of the models is required in order for them to reproduce the observed M_{bh} versus σ relationship. In particular, it is required that the outflows carry a relatively large proportion of the available accretion power of the AGN (~ 5 – 10 per cent; Fabian 1999; di Matteo et al. 2005, but see Hopkins & Elvis 2010). *Clearly, it is important to use direct observations to determine whether this fine-tuning is justified: are the AGN-driven outflows in ULIRGs truly as important as many of the simulations require?*

In line with the expectations of the hydrodynamic simulations, spectroscopic evidence for outflows has now been found in several ULIRGs using optical observations of neutral Na I D absorption lines (Rupke, Veilleux & Sanders 2005a,b; Rupke & Veilleux 2011), and far-IR/sub-mm observations of the molecular OH and CO lines (Feruglio et al. 2010; Fischer et al. 2010; Sturm et al. 2011). However, the evidence for a clear link between these outflows and nuclear AGN activity is mixed. For example, although the mass outflow rates and kinetic powers associated with the neutral Na I D

absorption line outflows are significant, comparisons between the properties of the neutral outflows in objects with and without optical AGN show surprisingly little difference (Rupke, Veilleux & Sanders 2005c). Moreover, while the results of Sturm et al. (2011), based on *Herschel* data, do suggest that the molecular outflows may be faster and more powerful in ULIRGs hosting powerful AGN (Sturm et al. 2011), the sample is small (only six objects) and incomplete.

It is important to recognize that the gas associated with any AGN-driven outflow may be highly ionized and therefore not adequately sampled by Na I D absorption and molecular line studies. In addition, the quantitative estimates of the properties of the neutral and molecular outflows are compromised by the fact that, in most cases, the radial extents of these outflows are not well constrained by the observations, which sample gas along the line of sight.

Results based on the optical studies of the large-scale (>5 kpc) warm ionized gas in ULIRGs (Heckman, Armus & Miley 1990; Soto & Martin 2012; Soto et al. 2012; Westmoquette et al. 2012) reveal a similar picture to the molecular and neutral gas studies: energetically significant outflows, but no clear differences between the outflows in ULIRGs with and without AGN; again, it is not clear whether the large-scale emission line gas is truly sampling the AGN-driven outflows. However, optical and mid-IR spectroscopic observations have recently revealed highly ionized outflows in the *near-nuclear regions* of several ULIRGs with Seyfert-like nuclei in the form of broad, blueshifted emission line components (Wilman, Crawford & Abraham 1999; Holt, Tadhunter & Morganti 2003; Lıpari et al. 2003; Holt et al. 2006; Spoon et al. 2009; Spoon & Holt 2009). These observations also suggest that the near-nuclear outflows are highly stratified (Holt et al. 2003; Spoon & Holt 2009), and that relativistic jets may play an important role in accelerating the gas (Holt, Tadhunter & Morganti 2009; Spoon & Holt 2009). Given that they isolate the AGN-driven outflow components, the near-nuclear high-ionization emission lines thus provide a powerful tool for addressing the key questions surrounding AGN-driven outflows in ULIRGs. These questions include the following.

(i) What is the dominant outflow driving mechanism in ULIRGs: AGN or starbursts? As discussed above, previous studies based on observations of the molecular, neutral and large-scale ionized gas outflows have not provided a clear-cut answer to this question. Clearly it is important to consider this question in the context of the near-nuclear warm outflows.

(ii) Are AGN-driven outflows more significant in Seyfert-like ULIRGs than in other types of AGN? Given that the ULIRGs are among the most actively evolving galaxies in the local Universe, with (predicted) high nuclear accretion rates, we might expect the AGN-induced outflows in such objects to be unusually strong. However, a large proportion of AGN of all types show evidence for outflows at some level, in the form of blue wings to the [O III] emission lines (e.g. Heckman et al. 1981; Whittle 1985; Veilleux 1991b; Nelson & Whittle 1995). Therefore, it is important to establish whether the outflows in Seyfert-like ULIRGs are significantly more extreme than those detected in the general population of non-ULIRG AGN.

(iii) What is the nature of the near-nuclear outflows in ULIRGs? Comparisons of spectroscopic observations of emission lines of different ionization have provided evidence that the near-nuclear emission lines outflows in some ULIRGs are stratified. However, it is currently uncertain whether the outflows comprise a small number of distinct outflow velocity components, each associated

Table 1. The sample of 17 ULIRGs discussed in this paper. These objects were selected from the Rodríguez Zaurín et al. (2009) ES sample of 36 ULIRGs and are classified as Sy2 in at least two of the three of the Kewley et al. (2006) diagnostic diagrams, or have Sy1 spectra. Column (1): object designation in the *IRAS* Faint Source Catalogue (FSC) Database. For those sources with multiple nuclei, the individual nucleus considered for this study is indicated in the table (N = north, S = south, E = east and W = west). Column (2): optical redshifts from Kim & Sanders (1998). Columns (3) and (4): right ascension (hours, minutes and seconds) and declination (degrees, arcminutes and arcseconds) of the *IRAS* source positions as listed in the Faint Source Database (FSCDB). Column (5): IR luminosity from Kim & Sanders (1998) adapted to our cosmology. Column (6): total [O III] λ 5007 emission line luminosities obtained from our modelling results (see the text for details). Column (7): 1.4 GHz monochromatic radio luminosities ($L_{1.4\text{ GHz}}$).

Name <i>IRAS</i> FSC	z	RA (J2000.0)	Dec. (J2000.0)	L_{IR} (W)	$L_{[\text{O III}]}$ (W)	$L_{1.4\text{ GHz}}$ (W Hz $^{-1}$)
(1)	(2)	(3)	(4)	(5)	(6)	(7)
F00188–0856	0.128	00 21 26.5	–08 39 26	9.2E+38	2.1E+33	6.8E+23
F01004–2237	0.117	01 02 51.2	–22 21 51	7.5E+38	1.6E+34	4.4E+23
F12072–0444	0.129	12 09 45.4	–05 01 14	9.4E+38	5.4E+34	3.3E+23
F12112+0305	0.073	12 13 46.0	02 48 38	8.2E+38	1.6E+33	5.7E+23
F13305–1739	0.148	13 33 15.2	–17 55 01	6.8E+38	4.4E+35	2.6E+24
F13428+5608	0.037	13 44 41.8	55 53 14	5.3E+38	9.0E+33	4.6E+23
F13451+1232E	0.122	13 47 33.3	12 17 24	8.0E+38	1.2E+35	1.9E+26
F14394+5332E	0.104	14 41 04.3	53 20 08	4.7E+38	4.1E+34	1.0E+24
F15130–1958	0.109	15 15 55.6	–20 09 18	5.3E+38	3.7E+34	2.7E+23
F15462–0450	0.100	15 48 56.8	–04 59 34	6.2E+38	3.4E+34	3.1E+23
F16156+0146NW	0.132	16 18 08.2	01 39 21	4.7E+38	6.0E+34	3.6E+23
F17044+6720	0.135	17 04 28.4	67 16 23	5.8E+38	1.9E+34	4.9E+23
F17179+5444	0.147	17 18 55.1	54 41 50	6.8E+38	5.0E+34	1.7E+25
F23060+0505	0.173	23 08 34.2	05 21 29	1.2E+39	1.0E+35	5.0E+23
F23233+2817	0.114	23 25 48.7	28 34 19	4.3E+38	7.8E+34	2.1E+23
F23327+2913S	0.107	23 35 11.9	29 30 00	4.9E+38	5.5E+33	2.1E+23
F23389+0300N	0.145	23 41 31.1	03 17 31	5.3E+38	2.7E+34	4.3E+25

with a particular spatial location and set of physical condition (Holt et al. 2003), or rather encompass a continuous gradient of velocities and physical conditions across the full extent of the emission-line region (e.g. De Robertis & Osterbrock 1986). At the same time it is important to confirm using a wide range of emission lines that the outflows are indeed decelerating, as suggested by observations of the mid-IR fine structure neon lines (Spoon & Holt 2009).

(iv) Do relativistic jets play an important role in accelerating the ULIRG outflows? Although it is certainly the case that some of the most extremely blueshifted emission line components are found in ULIRGs that contain powerful relativistic jets (Holt et al. 2003, 2006), the issue of the jet contribution to the acceleration and ionization of the outflows warrants further investigation using a complete sample of ULIRGs that is unbiased towards jet properties.

(v) How energetically significant are the AGN-induced outflows in ULIRGs? In terms of testing the hydrodynamical merger simulations that incorporate AGN feedback as a key element, it is crucial to accurately quantify the mass outflow rates and kinetic powers of the near-nuclear outflows. In this way it will also be possible to compare the properties of the near-nuclear AGN outflows with those of the neutral and large-scale ionized gas outflows, to determine whether the AGN-induced outflows are truly energetically significant.

In this paper, we directly address these questions using detailed optical spectroscopic observations of a complete sample of 17 nearby ($z < 0.175$) ULIRGs with Seyfert-like nuclear spec-

tra. Throughout this paper, we assume a cosmology with $H_0 = 71 \text{ km s}^{-1} \text{ Mpc}^{-1}$, $\Omega_0 = 0.27$, $\Omega_\Lambda = 0.73$.

2 SAMPLE SELECTION, OBSERVATIONS AND DATA REDUCTION

In order to achieve the aims of this project, we require a sample of ULIRGs with Seyfert-like nuclear spectra that are close enough to study in detail and have high quality nuclear spectra; the sample also needs to be complete as possible. As a starting point, we took the ‘Extended Sample’ (ES) of Rodríguez Zaurín et al. (2009), which comprises 36 nearby ($z < 0.175$) ULIRGs of all spectral types from the 1 Jy sample of Kim & Sanders (1998) that have deep William Herschel Telescope (WHT) spectra. We then selected all the objects with Seyfert-like nuclear spectra from this sample. To make this selection, we use the criteria of Yuan, Kewley & Sanders (2010), which in turn are based on the emission line diagnostic diagrams of Kewley et al. (2006) for SDSS galaxies. Specifically, we selected all the objects classified as Sy2 in at least two out of three of the Kewley et al. (2006) diagnostic diagrams, as well as the three objects with broad-line Seyfert 1 spectra. This results in a sample of 19 nearby ULIRGs with Seyfert-like spectra, redshifts $z < 0.175$, declinations $\delta > -25$, and right ascensions $12 < \text{RA} < 02 \text{ h}$ (see Table 1 for details). In comparison, a total of 22 ULIRGs from the full 1 Jy sample of Kim & Sanders (1998) meet the same selection criteria in optical classification, redshift, declination and right ascension, and of these only three objects – F12265+0219 (3C 273), F13443+08, F14121–0126 – are not included in our sample of

ULIRGs with Seyfert-like nuclear spectra and deep WHT spectra. Therefore, our sample is 86 per cent complete,¹ and is certainly representative of the subset of ULIRGs with optical Seyfert nuclei in the local Universe.

As described in Rodríguez Zaurín et al. (2009), deep spectra of all of the 19 objects in our sample were taken with the ISIS dual-beam spectrograph on the 4.2 m WHT, on La Palma, Spain. The observations were carried out using the R300B grating with the EEV12 CCD, and the R316R grating with the MARCONI2 CCD on the blue and the red arm, respectively. The instrumental setup resulted in a spatial scale of $0.4 \text{ arcsec pixel}^{-1}$ for both arms, and a dispersion of $1.72 \text{ \AA pixel}^{-1}$ for the blue and $1.65 \text{ \AA pixel}^{-1}$ for the red arm. The useful wavelength range is $\sim 3300\text{--}7800 \text{ \AA}$, in the observed frame. A slit of width 1.5 arcsec was used for all the objects. In order to minimize the effects of differential atmospheric refraction, the objects were observed either with the slit aligned along the parallactic angle, or at small airmass ($AM < 1.1$). Although we lack accurate seeing estimates for individual objects, because ISIS/WHT does not provide imaging observations, measurements by the DIMM seeing monitor at the observatory suggest that the seeing was in the range $0.6 < FWHM < 2.6 \text{ arcsec}$, and usually less than 2.0 arcsec , for the nights of the observations.

The data were reduced (bias-subtracted, flat-field-corrected, cleaned of cosmic rays, wavelength-calibrated, flux-calibrated and straightened) before extraction of the individual spectra using the standard packages in IRAF and the STARLINK packages FIGARO and DIPSO. The wavelength-calibration accuracy, measured as the mean shift between the measured and published (Osterbrock et al. 1996) wavelength of night-sky emission lines, is $\sim 0.35 \text{ \AA}$ for the blue spectra and $\sim 0.25 \text{ \AA}$ for the red spectra. The spectral resolutions, calculated using the widths of the night-sky emission lines (FWHM), are in the ranges $4.9\text{--}5.6$ and $5.1\text{--}5.5 \text{ \AA}$ for the blue and red arms, respectively. Finally, the estimated uncertainty for the relative flux calibration is ± 5 percent, based on comparison of the response curves of several spectrophotometric standard stars observed during all the observing runs.

Following reduction, inspection of the spectra revealed that in two of the three objects with Seyfert 1 spectra (Mrk 231, F21219–1775), the strength the broad Balmer and Fe II emission features and non-stellar continuum prevented analysis of their narrow-line emission. Therefore, we excluded these two objects from further analysis. Note however that although it has not proved possible to study the narrow emission line kinematics in the nucleus of the two excluded Seyfert 1 objects, one of these objects – Mrk 231 – is well known to show evidence for outflows based on absorption line studies of the neutral and molecular gas, and the extended emission-line regions (e.g. Rupke & Veilleux 2011). Overall our final sample comprises 17 Seyfert-like ULIRGs with viable spectra.

3 RESULTS

In this paper, we are interested in the AGN-induced outflows in the near-nuclear regions of ULIRGs. Therefore, we concentrate on the 5 kpc-diameter nuclear apertures described in the Rodríguez Zaurín et al. (2009, 2010) stellar population study of the galaxies. In this section, we describe the results obtained by fitting the profiles of the emission lines detected in the nuclear spectra.

¹ This rises to 90 per cent if we exclude from consideration the powerful quasar F12265+0219 (3C 273), which is dominated by non-thermal jet emission, rather than thermal dust emission, at infrared wavelengths.

3.1 Fitting the emission line profiles

Prior to the modelling of the emission line profiles in the nuclear regions, the spectra were shifted to the galaxy rest frame and a continuum model was subtracted from the data. In each case, the continuum model was selected among the best-fitting models to the stellar continuum emission from the galaxy (see Rodríguez Zaurín et al. 2009 for details on the stellar continuum modelling technique).

Once the continuum emission was subtracted, we used the DIPSO package to fit Gaussian profiles to the emission lines. Our general modelling philosophy was to fit each emission line with the minimum number of Gaussian components required to produce an acceptable fit.² The velocity widths derived from the fits were quadratically corrected for the instrumental profile, and all line widths and radial velocity shifts were corrected to the rest frames of the objects.

One of key aspects we want to investigate is the nature of the outflows: whether they comprise a small number of distinct outflow velocity components, each associated with a particular spatial location and set of physical conditions (e.g. Villar-Martín, Binette & Fosbury 1999; Holt, Tadhunter & Morganti 2008), or on the contrary, there is a continuous gradient of velocities and physical conditions across the full extent of the emission-line region (e.g. Holt et al. 2003; Spoon & Holt 2009). In the first scenario, one kinematic model would provide an adequate fit to all the different emission lines, while in the second scenario each line would have different kinematic components.

To test these scenarios, it is first necessary to select a prominent emission line that is suitable to generate a model that will be used to fit all the other emission lines. In this context, the strong [O III] $\lambda\lambda 4959, 5007$ lines usually have high S/N in our spectra, are in a region clean from any atmospheric absorption, and are not blended with other emission lines (as in the case of H α and [N II] $\lambda\lambda 6548, 6583$ or the [O II] $\lambda\lambda 3727, 3729$ doublet). Therefore, where possible, we started the individual analysis of each source by fitting the [O III] $\lambda\lambda 4959, 5007$ emission lines. When fitting these lines we used three constraints in accordance with atomic physics: (i) the flux ratio between [O III] $\lambda 4959$ and [O III] $\lambda 5007$ was set at 2.99:1 (based on the transition probabilities); (ii) the widths of the corresponding kinematic components of each line were forced to be equal; (iii) the shifts between the corresponding components of each line were fixed to be 48.0 \AA . We will refer to this as ‘the [O III] model’ hereafter.

We then attempted to model the other prominent emission lines in the spectra with the same kinematic model (velocity widths and shifts) as [O III], leaving the relative fluxes in the kinematic sub-components to vary. As well as the constraints derived from the [O III] model, it is possible to further constrain the fits to other doublets in accordance with atomic physics: the shifts between the corresponding components of each line in all doublets (e.g. [Ne III] $\lambda\lambda 3868, 3968$, [Ne V] $\lambda\lambda 3346, 3425$, [N II] $\lambda\lambda 6548, 6583$, [O I] $\lambda\lambda 6300, 6363$ and [S II] $\lambda\lambda 6716, 6731$) were set, and for some doublets (e.g. [Ne III] $\lambda\lambda 3868, 3968$, [Ne V] $\lambda\lambda 3346, 3425$, [N II] $\lambda\lambda 6548, 6583$ and [O I] $\lambda\lambda 6300, 6363$) the flux ratios were set based on the transition probabilities. For [S II] $\lambda\lambda 6716, 6731$, the flux ratio was required to be within the range $0.44 < [S II](6716/6731) < 1.42$, which covers the predicted variation in the ratio between the high- and low-density

² We define a ‘acceptable’ fit to a emission line based on visual inspection, i.e. one that has acceptable low residuals and adequately represents the overall shape of the line profiles.

limits. For simplicity, the [O II] $\lambda\lambda 3726, 3728$ lines were treated as a single line for the majority of the objects in our sample.³ Therefore, in those cases we assumed 3727.0 \AA as the rest-frame wavelength.

The [O III] modelling technique was successful for all but 4 of the 17 objects in the sample discussed in this paper (~ 76 per cent). This is consistent with the idea that, in the majority of cases, there exist a discrete number kinematic components, each with its own line width, velocity shift, physical conditions and ionization. However, in the cases of F13451+1232, F14394+5332, F16156+0146 and F23389+0300 (~ 24 per cent of the objects in our sample), it was not possible to use a single model to fit all the emission lines observed in their optical spectra, suggesting that there may be a continuous gradient of density, ionization and kinematics through the narrow-line region (NLR), leading to each line having a different profile.

Fig. 1 shows the fits to the [O III] emission lines profile for all but three of the objects in our sample. In the cases of F00188–0856 and F23327+2913, the [O III] $\lambda\lambda 4959, 5007$ emission lines have a low equivalent width and the profiles are affected by residual structure in the underlying continuum; hence, it is not possible to precisely fit these lines. However, it is still possible in these cases to find one kinematic model that fits all emission lines, based on the stronger $H\alpha + [N II]$ lines. Fig. 1 shows the fits to the $H\alpha + [N II]$ complex for these two objects. In addition, a detailed study of the kinematics for F13451+1232 is presented in Holt et al. (2003, 2011), including the fit to the [O III] emission line. Therefore, no fit for this source is shown in Fig. 1. Table 2 presents the widths and shifts of the different kinematic components for the [O III] model (or $H\alpha + [N II]$ model in two cases) for the central 5 kpc aperture for all galaxies in our sample, whereas Table 3 presents the line fluxes and emission line ratios.

We emphasize that the fits to some emission line blends have the potential to suffer from degeneracies, in the sense that it is possible for the fitting programme to allocate the fluxes between the different kinematic components in various ways and still produce acceptable fits to the overall emission line profile. This is a particular problem in cases where there are multiple, broad kinematic components, and the components of the blend are relatively close together in wavelength (e.g. $H\alpha + [N II]$ $\lambda\lambda 6548, 6584$ and $[S II]$ $\lambda\lambda 6717, 6731$). To check whether the degeneracy is a consequence of the particular fitting program (DIPSO) we have used, we have also modelled the emission line profiles of those objects for which the degeneracies were more important (e.g. F01004–2237 or F15130–1958) using the MPFIT code (Markwardt 2009). The main difference between DIPSO and MPFIT is that whereas DIPSO fits the kinematic components in each individual emission line or blend individually, MPFIT fits all the lines/blends in the spectrum simultaneously. Overall, the MPFIT results were consistent with those obtained using DIPSO and the degeneracies were still present. The impact of these potential degeneracies on the fits to emission line blends in individual objects is discussed in the Appendix.

As well as fitting the 17 objects in our sample of ULIRGs with optical Seyfert nuclei, for the purposes of comparison, we used identical techniques to fit the [O III] $\lambda\lambda 4959, 5007$ and/or $H\alpha + [N II]$ profiles in the 5 kpc aperture nuclear spectra of the 16 nearby

ULIRGs in the ES ($z < 0.175$) of Rodríguez Zaurín et al. (2009) that do not show evidence for Seyfert nuclei at optical wavelengths.

For ease of reference in the following sections, we use the following scheme to label kinematic components, based on line widths (FWHM):

- (i) narrow: $\text{FWHM} < 500 \text{ km s}^{-1}$;
- (ii) intermediate: $500 < \text{FWHM} < 1000 \text{ km s}^{-1}$;
- (iii) broad: $1000 < \text{FWHM} < 2000 \text{ km s}^{-1}$;
- (iv) very broad $2000 \text{ km s}^{-1} > \text{FWHM}$.

Detailed descriptions of the line profile fits for individual ULIRGs are described in the Appendix, while in the following sections we describe the general results derived from these fits.

3.2 The incidence of kinematically disturbed components in Seyfert and non-Sy-ULIRGs

Kinematic disturbance of the emission line gas does not necessarily involve large line shifts, but can also be indicated by large line widths in components that are relatively unshifted. Therefore, we define the term ‘kinematic disturbance’ in this paper to encompass kinematic components that have intermediate or broad line widths ($\text{FWHM} > 500 \text{ km s}^{-1}$) and/or large blueshifts relative to the galaxy rest frame ($\Delta V < -150 \text{ km s}^{-1}$). By this definition, the overwhelming majority (16/17 or 94 per cent) of the Sy-ULIRGs for which we have been able to measure the emission line profiles in this study show evidence for kinematic disturbance in their nuclear regions. In contrast, only a small minority (3/16 or ~ 19 per cent) of the non-Sy-ULIRGs from Rodríguez Zaurín et al. (2009) present evidence for kinematic disturbance in the nuclear 5 kpc apertures.⁴ This difference is significant at the $\sim 3\sigma$ level, strongly suggesting that the kinematically disturbed components are driven by the AGN in most cases, rather than by the circumnuclear starbursts. Significantly, the one Sy-ULIRG that shows no clear signs of nuclear kinematic disturbance – F12112+0305 – is also the object that presents the weakest evidence for Seyfert-like AGN activity based on its line ratios – falling close to the AGN/H II composite region in the diagnostic diagrams of Yuan et al. (2010); it also has the lowest [O III] emission line luminosity of all the Sy-ULIRGs in our sample (see Table 1).

At first sight these results may seem in contrast with those of Soto & Martin (2012) and Soto et al. (2012) who studied a sample of 39 ULIRGs and found evidence for disturbed kinematics in the majority of the objects in their sample, which is dominated by non-Sy ULIRGs. However, the Soto & Martin (2012) spectroscopic data set has higher spectral and spatial resolution than ours. In addition, the sizes of the extraction apertures are different from those used in this paper. Therefore, it is likely that they detect some broad components that are not observed in our spectra. Finally, Soto & Martin (2012) and Soto et al. (2012) used a different modelling approach from the one we use here (i.e. a ‘simplest model approach’). As a result, their kinematic models for the nuclear emission lines in some of the sources in their sample comprise more than one kinematic component, regardless of whether the additional components are actually required to produce an adequate fit.

³ There are three cases (F12072–0444, F17044+6720 and F17179+5444) for which accounting for the doublet nature of at least one of the different kinematic components was necessary to adequately model the [O II] $\lambda\lambda 3726, 3729$ emission lines.

⁴ These three ULIRGs are F14348–1447, F23234+0946 and F15327+2340.

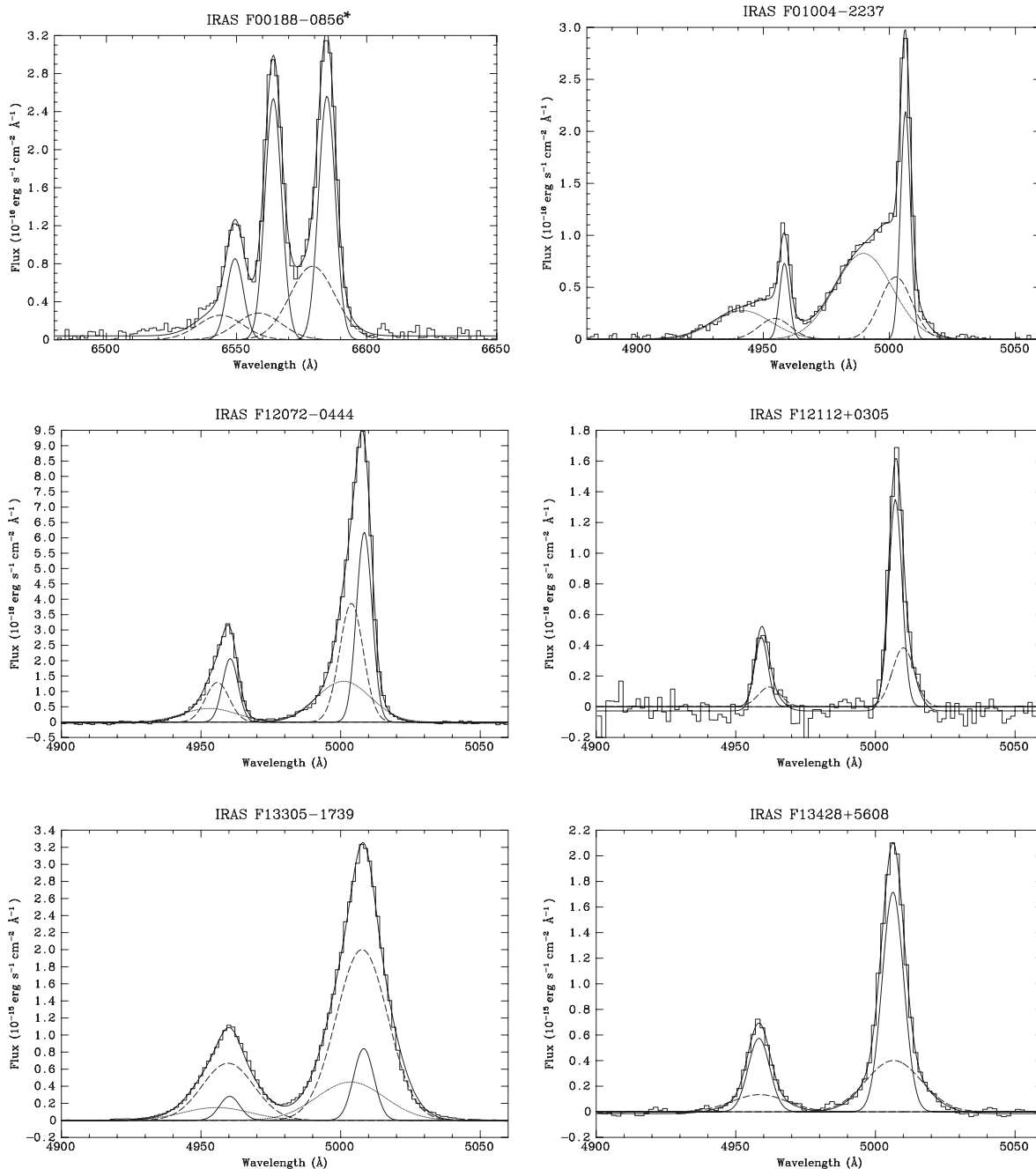
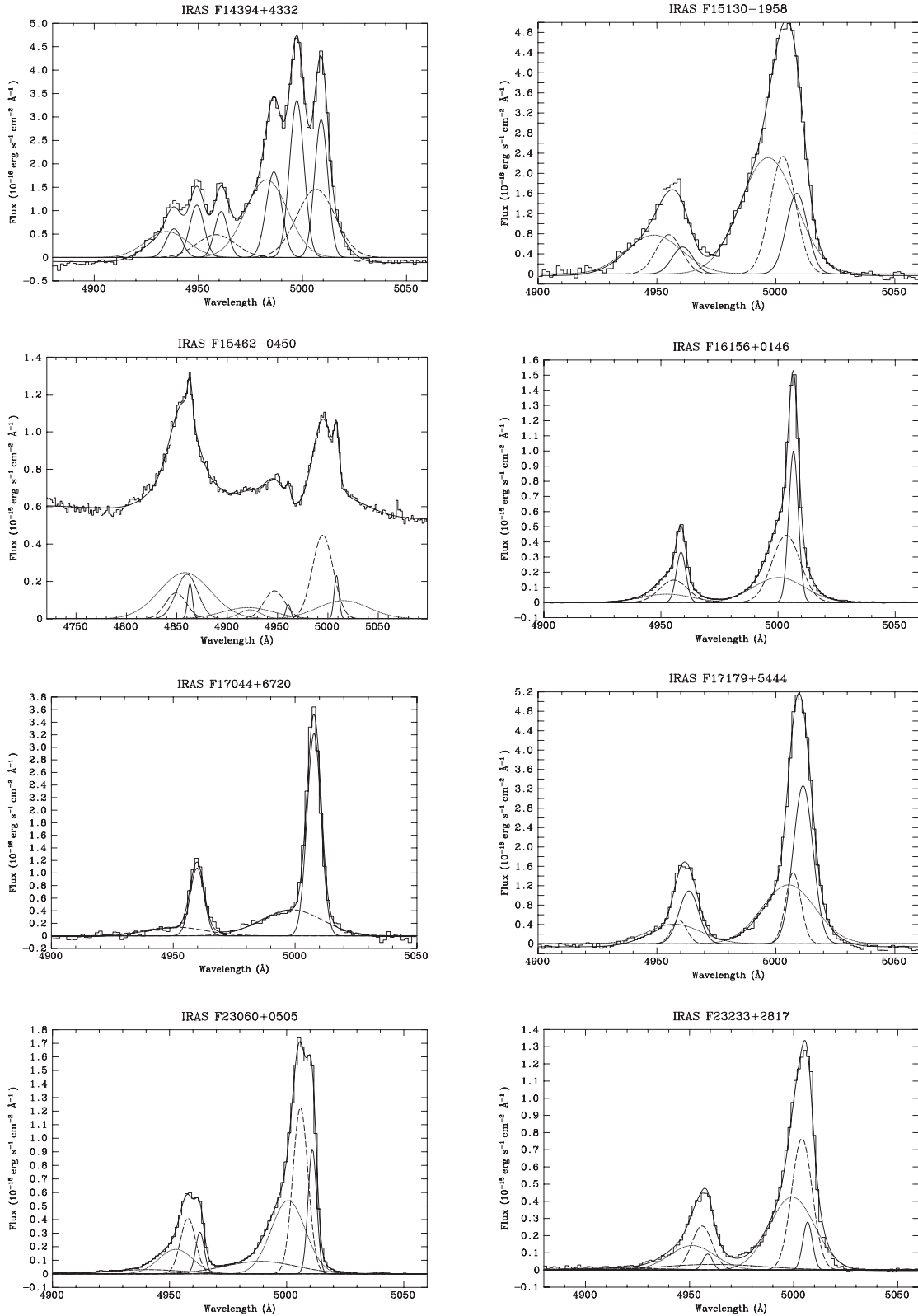


Figure 1. Fits to the [O III] emission lines profile of all the objects in our sample, with the exception of IRAS F13451+1232, IRAS F00188-0856 and IRAS F23327+2913. In the case of IRAS F13451+1232, the fit to the [O III] profile can be found in Holt et al. (2003) and therefore is not included in the figure. In the latter two cases, the [O III] emission lines have low equivalent widths and we used the H α + [N II] complex to find one model that reproduces all emission lines. In each case, the best-fitting model is overplotted (bold line) on the extracted spectrum (faint line). The different kinematic components are also plotted in the figure. The narrow, intermediate, broad and very broad (if present) components correspond to the solid line, dashed line, dotted line and dot-dashed line. The exceptions are IRAS F13305-1739, IRAS F15130-1958 and IRAS 23060+0505. In the first case, the dashed line corresponds to one of the two broad components detected in this object, referred to as B1 in Table 2. In the case of IRAS F15130-1958, the solid line corresponds to the intermediate component referred to as I1 in Table 2. Finally, in the case of IRAS 23060+0505, the dashed line corresponds to the narrow component referred to as N2 in Table 2. In addition, IRAS F14394+5332 shows a spectacular [O III] profile that is not observed in all the other emission lines detected in its spectrum. See Notes (in Appendix) on individual sources for details of the modelling for this and the other ULIRGs in our sample.

3.3 The diversity of emission line profiles

Fig. 1 and Table 2 demonstrate a striking diversity in the emission line profiles of Sy-ULIRGs. The profiles range from the complex,

multicomponent profile visible in F14394+5332, through the case of IRAS F17044+6720, in which there is a single broad, blueshifted component along with a strong narrow component, to the case of F23389+0300, which has a strong and extremely broad component

Figure 1 – *continued*

that makes up a large proportion of the flux, yet is barely shifted relative to the narrow component. The minimum number of Gaussian components required to fit the individual emission lines ranges from 2 to 5, with seven objects (~ 41 per cent) requiring two, seven objects

(~ 41 per cent) requiring three, two objects (~ 12 per cent) requiring four and one object (F14394+5332) requiring five components for an adequate fit. However, it is important to note that, in the two cases – F23060+0505 and F23233+2817 – where a fourth component is

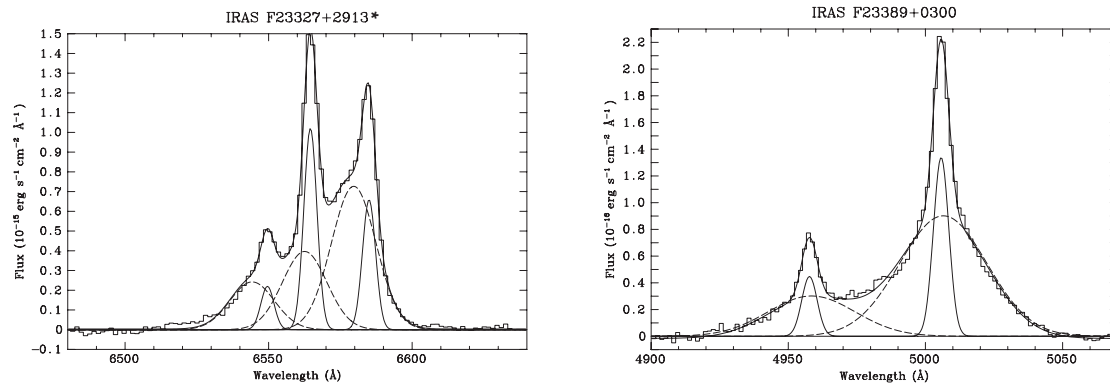


Figure 1 – continued

Table 2. The FWHM and velocity shifts (ΔV) for the different kinematic components of the galaxies in our sample. Column (1): object name. Column (2): the label of the different components as defined in the previous section [N (narrow), I (intermediate), B (broad) and VB (very broad)]. For those objects with two components within the same FWHM range, these are indicated with numbers (e.g. B1 and B2 corresponding to the two broad components detected in IRAS F13305–1739). Columns (3) and (4): rest-frame widths (FWHM) and shifts relatively to galaxy rest frame (ΔV) of the different components.

Object		FWHM	ΔV
IRAS		(km s ⁻¹)	(km s ⁻¹)
(1)	(2)	(3)	(4)
F00188–0856	N	269 ± 14	
	I	904 ± 79	–253 ± 36
F01004–2237	N	Unres	
	I	849 ± 79	–229 ± 32
	B	1590 ± 94	–999 ± 80
F12072–0444	N	275 ± 18	
	I	525 ± 36	–276 ± 30
	B	1343 ± 84	–446 ± 35
F12112+0305	N1	162 ± 73	
	N2	473 ± 66	–171 ± 14
F13305–1739	N	435 ± 29	
	B1	1275 ± 31	–36 ± 14
	B2	1685 ± 286	–281 ± 29
F13428+5608	N	450 ± 13	
	B	1368 ± 66	+14 ± 11
F13451+1232	N	340 ± 23	
	B1	1255 ± 41	–402 ± 9
	B2	1944 ± 65	–1980 ± 36
F14394+5332	N1	335 ± 26	
	N2	390 ± 32	–700 ± 10
	N3	435 ± 52	–1358 ± 18
	B1	1272 ± 67	–156 ± 8
	B2	1401 ± 131	–1574 ± 19
F15130–1958	I1	545 ± 85	
	I2	700 ± 222	–350 ± 281
	B	1630 ± 42	–725 ± 131
F15462–0450	N	147 ± 57	
	B	1426 ± 39	–822 ± 25
F16156+0146	N	Unres	
	I	804 ± 26	–186 ± 10
	B	1535 ± 63	–374 ± 26
F17044+6720	N	290 ± 20	
	B	1765 ± 103	–553 ± 65

Table 2 – continued

Object		FWHM	ΔV
IRAS		(km s ⁻¹)	(km s ⁻¹)
(1)	(2)	(3)	(4)
F17179+5444 ^a	N	358 ± 75	–123 ± 33
	I	515 ± 33	123 ± 34
	B	1562 ± 43	–242 ± 61
F23060+0505	N1	376 ± 10	–152 ± 6
	N2	Unres	152 ± 4
	B	1001 ± 23	–463 ± 20
	VB	2150 ± 125	–1073 ± 122
F23233+2817	N	178 ± 37	
	I	640 ± 24	–161 ± 15
	B	1511 ± 118	–447 ± 40
	VB	3433 ± 903	–2706 ± 422
F23327+2913	N	109 ± 12	
	I	804 ± 14	–94 ± 4
F23389+0300	N	289 ± 12	
	VB	2223 ± 30	47 ± 13

^aTwo models adequately reproduced the emission lines in the case of F17179+5444. One model comprises a narrow, an intermediate and a broad component, while the second model includes two narrow components plus a broad one. The results shown in the table for this galaxy correspond to the first model. For details on the modelling for this and all the other objects in our sample, see Section 3.2.

required to adequately model the emission lines, the relative flux contribution of this fourth component is relatively small. Therefore, its FWHM and shift with respect to the narrow component are relatively unconstrained.

In terms of determining the direction and magnitude of the velocity shift of any kinematically disturbed component, it is important to carefully determine the rest-frame velocities of the ULIRG host galaxies (see Holt et al. 2003, 2006, 2008). In the absence of other indicators (e.g. accurate stellar kinematics), the best way to do this is to compare the kinematics of the extended narrow components along the slit with the various kinematic components detected in the spatially integrated emission line profile of the 5 kpc aperture. For example, if the undisturbed gas shows a rotation curve across the nucleus, the component in the spatially integrated emission line profile that corresponds to the galaxy rest frame will have a wavelength corresponding to the centroid of the blue and redshifted components on either side of the nucleus. In the majority of the cases in which

Table 3. The fluxes of various emission lines detected in the optical spectra of the sources. Column (1): object name. Column (2): the label of the different components (same as Column (2) in Table 2). Column (3): $H\beta$ flux in $\text{erg s}^{-1} \text{cm}^{-2}$. From Columns (4)–(9) and columns (11) and (12): ratios of the fluxes of the main emission lines to the $H\beta$ line. The uncertainties in these ratio are typically $\lesssim 15$ per cent, as estimated accounting for the 5 per cent flux calibration uncertainty, and the uncertainties in the model fits themselves. However, there are a few particular cases, mainly the broadest component in some emission lines, or those kinematic components that make a small contribution to the flux, for which the uncertainty can be as high as 50 per cent (for example, the I2 component of the $[S\text{ II}] \lambda\lambda 6716, 6731$ emission lines in the case of IRAS F15130–1958). Column (10): uncertainties in the $H\alpha/H\beta$ ratio (we discuss in the text a possible correlation between the broadness of the different kinematic components and their corresponding reddening. Therefore, it is particularly important to give the uncertainties associated with this ratio explicitly).

Object		$H\beta$	$[\text{Ne v}] \lambda 3426$	$[\text{O II}] \lambda 3727$	$[\text{Ne III}] \lambda 3869$	$[\text{O III}] \lambda 5007$	$[\text{O I}] \lambda 6300$	$H\alpha$	$\Delta(H\alpha/H\beta)$	$[\text{N II}] \lambda 6583$	$[\text{S II}] \lambda\lambda 6716, 6731$
IRAS		($\text{erg cm}^{-2}\text{s}^{-1}$)									
(1)	(2)	(3)	(4)	(5)	(6)	(7)	(8)	(9)	(10)	(11)	(12)
F00188–0856	N	2.92E–16	–	1.96	–	0.40	0.97	6.97	0.93	7.03	–
	I	1.76E–16	–	3.01	–	2.00	0.38	3.46	1.07	9.54	–
F01004–2237	N	4.03E–16	–	1.21	0.25	2.66	0.29	4.01	0.24	0.99	1.00
	I	4.60E–16	–	1.85	0.55	2.07	0.42	4.45	0.72	1.90	0.46
	B	3.65E–16	–	0.62	0.94	6.47	0.40	2.51	0.51	7.47	1.17
F12072–0444	N ^a	1.23E–15	0.02	2.78	0.27	3.50	0.70	5.91	0.13	3.71	–
	I	4.82E–16	0.69	1.70	0.67	8.47	0.47	5.48	0.61	6.46	–
	B	4.68E–16	0.09	1.26	0.79	6.92	1.07	6.75	0.92	6.30	–
F13305–1739	N	1.67E–15	0.46	0.65	0.20	4.61	0.06	3.37	0.46	1.59	1.24
	B1	4.57E–15	0.62	1.67	0.95	10.15	0.71	3.74	0.70	5.83	1.88
	B2	9.69E–16	–	2.03	1.97	14.06	0.85	8.35	5.60	4.98	1.20
F13428+5608	N	8.38E–15	–	1.37	–	1.98	0.66	5.67	0.19	4.09	3.36
	B	9.02E–16	–	10.34	–	11.80	2.65	9.81	3.80	29.36	6.94
F13451+1232 ^b	N	5.85E–16	0.02	3.24	0.30	2.34	0.89	3.32	0.33	4.76	3.79
	B1	2.11E–15	0.01	1.34	0.65	9.37	1.10	5.16	0.28	6.27	1.83
	B2	3.24E–16	1.22	0.55	4.81	24.42	7.31	18.81	4.74	1.98	6.50
F14394+5332 ^b	N	2.88E–15	–	1.32	0.02	0.63	0.49	6.61	0.17	3.14	2.69
	B	8.06E–16	–	16.81	2.88	15.12	6.25	17.59	5.02	27.82	16.14
F15130–1958	I1	6.06E–16	0.13	2.91	0.30	2.91	1.03	4.24	0.42	8.04	3.21
	I2	2.47E–16	1.21	3.05	1.97	12.73	0.85	3.99	0.89	11.96	0.27
	B	4.51E–16	3.69	1.57	3.09	15.05	1.41	4.01	0.85	12.04	2.97
F15462–0450 ^c	N	1.11E–15	0.38	3.59	0.38	1.23	–	7.47	0.75	2.74	2.81
	B	3.56E–15	0.58	0.85	0.95	3.25	–	–	–	–	0.85
	BLR	2.20E–14	–	–	–	–	–	4.79	0.20	–	–
F16156+0146 ^b	N	5.62E–16	0.49	0.21	0.84	9.06	0.17	4.04	0.48	0.51	–
	N/I	4.66E–16	0.15	6.30	0.05	14.43	1.65	6.26	1.54	3.93	–
	B	9.05E–16	0.28	1.29	0.78	5.05	0.88	5.71	0.80	4.33	–
F17044+6720	N ^a	1.25E–15	–	2.98	0.24	1.86	0.65	5.05	0.17	2.50	–
	B ^a	2.49E–16	–	4.26	–	5.27	1.48	5.33	2.89	14.13	–
F17179+5444 ^d	N ^a	7.82E–16	0.37	1.16	0.23	1.15	0.79	4.72	0.50	5.17	2.97
	I ^a	3.31E–16	–	6.42	1.32	10.24	0.43	5.89	2.27	4.36	0.84
	B	4.64E–16	–	–	0.18	7.40	0.77	7.71	2.04	9.37	2.46
F23060+0505 ^e	N1	1.83E–15	0.21	2.05	0.45	5.42	0.42	4.23	0.14	2.55	1.75
	N2	6.23E–16	0.23	1.24	0.97	6.76	0.24	2.30	0.26	0.84	0.50
	B	8.39E–16	1.28	2.19	1.00	11.96	0.36	8.11	0.85	7.40	2.83
F23233+2817 ^e	N	8.10E–16	0.45	1.28	0.42	1.98	0.33	5.12	0.69	5.66	2.37
	I	8.86E–16	0.88	2.59	1.26	10.68	0.63	4.46	1.12	13.37	1.41
	B	1.58E–15	1.10	0.41	1.14	7.34	0.40	2.10	0.33	4.99	1.04
F23327+2913 ^f	N	–	–	0.14	–	0.05	0.08	5.82E–15	0.65	0.47	–
	I	3.02E–15	–	0.91	–	0.62	0.26	2.55	0.14	4.68	0.75
F23389+0300 ^b	N/I	4.12E–16	–	3.33	0.28	2.28	4.88	7.87	1.02	4.71	2.52
	VB	9.88E–16	–	1.91	0.43	3.63	7.34	8.35	1.26	25.88	9.46

^aAs a first approach during the modelling, $[\text{O II}] \lambda\lambda 3726, 3729$ was treated as a singlet rather than a doublet. However, there are cases for which accounting for the doublet nature of at least one of the different kinematic components is necessary to adequately model the $[\text{O II}] \lambda\lambda 3726, 3729$ emission lines. The fluxes presented in the table for these cases are the sum of the two lines of the doublet. ^bFor these four galaxies, it was not possible to find one model that adequately reproduces all the emission lines. In the cases of IRAS F13451+1232, F16156+0146 and F23389+0300, the number of components is the same for all the emission lines, although with different widths and shifts. Therefore, it is still possible to use the $H\beta$ line as a reference and give line fluxes relative to that line. In the case of F14394+5332, the modelling results reveal the presence of a narrow component at rest frame found in *all* the emission lines, plus a number of different blueshifted components with different widths and shifts for the different emission lines. Therefore, to give an idea of the fluxes from the narrow component and the shifted components, we define two kinematic components in this case: narrow (N), corresponding to the narrow component found for all emission lines, and broad (B), which comprises the sum of all the kinematic components for each line that are not the narrow component. ^cThis is the only object with a strong broad-line Sy1 nucleus in our sample. Due to the large contribution of the broad component from the broad-line region (BLR) in the case of the $H\alpha$ emission, it is not possible to constrain the flux in the broad, blueshifted component detected in $[\text{O III}]$ (referred to as B in the table) for this particular emission line. Therefore, no flux value for the B component is presented in the table for this galaxy (see Appendix for details). ^dTwo models adequately modelled the emission lines in the case of F17179+5444. One model comprises a narrow, an intermediate and a broad components, while the second model includes two narrow components of the same width plus a broad one. The results shown in the table for this galaxy correspond to the first model. ^eThe very broad (VB) kinematic component for these two ULIRGs is only detected in high ionization emission lines (i.e. not in the case of $H\beta$) and therefore not included in the table. ^fThe $H\beta$ emission line for this galaxy falls close to the region of the spectrum that is heavily affected by the dichroic. Therefore, the narrow component, which makes a relative small contribution to most of the emission lines, is not detected in the case of $H\beta$. For this components line fluxes are given relative to $H\alpha$.

we have spatially resolved information on the narrow line kinematics, we find that the redmost narrow component in the spatially integrated profile coincides with the galaxy rest frame. However, in two cases – F17179+5444 and F23060+0505 – a narrow and a relatively low-FWHM intermediate component ($\text{FWHM} = 515 \pm 33 \text{ km s}^{-1}$), or two narrow components, are present in the nuclear line profiles, each corresponding to the velocity shift of the spatially resolved gas on one or other side of the nucleus. In these cases, the observed narrow line splitting is likely to represent unresolved rotation, or to trace a large-scale bipolar outflow in the gas (see, for example, Holt et al. 2008). In these two cases, we used the average of the wavelengths of the two narrow components to define the galaxy rest frame.

With the exceptions of F17179+5444 and F23060+0505, the velocity shifts listed in Table 2 are defined relative to the redmost narrow component fitted in the 5 kpc aperture spectrum. It is clear that the broadest kinematic components in each object are significantly blueshifted relative to the galaxy rest frames in all cases except F13428+5608 and F23389+0300. In the case that the emission line clouds suffer extinction by a general field of dust in the nuclear regions of the galaxies, rather than by dust in the clouds themselves, this implies that in most cases the gas is undergoing a radial outflow from the nucleus.

Finally, we can define the flux-weighted mean line width and velocity shift of the disturbed kinematic components as

$$\text{FWHM}_w = \frac{\sum_i (F_i \times \text{FWHM}_i)}{\sum_i F_i} \quad (1)$$

$$\Delta V_w = \frac{\sum_i (F_i \times \Delta V_i)}{\sum_i F_i}, \quad (2)$$

where F_i , FWHM_i and ΔV_i are the fluxes, FWHM and velocity shifts of all the intermediate and broad kinematic components with respect to the rest frame. The results are shown in Table 4. For our sample of 16 ULIRGs, we find values in the range of $797 \leq \text{FWHM}_w \leq 2223 \text{ km s}^{-1}$ with a mean and median values of 1253 and 1336 km s^{-1} , respectively. In the case of the ΔV_w we find values in the range $-942 < \Delta V_w < 47 \text{ km s}^{-1}$ with mean and median values of -406 and -333 km s^{-1} , respectively.

Fig. 2 shows FWHM_w and ΔV_w plotted against the total [O III] $\lambda 5007$ emission line luminosity ($L_{[\text{O III}]}$) from column 6 of Table 1. This figure is designed to investigate any possible correlation between the properties of the outflows and the AGN power, as indicated by the $L_{[\text{O III}]}$ luminosity, which is often considered to be a reliable AGN bolometric indicator (e.g. LaMassa et al. 2009, 2010; Dicken et al. 2010). However, we do not find any clear correlation between $L_{[\text{O III}]}$ and either the shifts or the widths of the outflows observed at optical wavelengths for the galaxies in our sample. Our results suggest that the kinematic properties of the AGN-induced outflows present in Sy-ULIRGs are not strongly dependent on the instantaneous AGN radiative power as indicated by the [O III] luminosity. A possible reason for this lack of a correlation is that the [O III] luminosity represents the AGN power on the time-scale of the light crossing time of the NLR ($t_{\text{NLR}} \lesssim 10^4 \text{ yr}$), but the AGN activity may be highly variable within the $\sim 10^8 \text{ yr}$ time-scale of the final stages of gas-rich mergers represented by the ULIRGs. In this case, the instantaneous [O III] luminosity might not provide a good indication of average AGN power over the entire activity cycle. Alternatively, because of the substantial extinction on a kpc-scale in the NLRs of ULIRGs, the [O III] luminosity may not be as reliable an indicator of the AGN bolometric luminosity as it is in other

Table 4. Weighted mean FWHM and velocity shifts (FWHM_w and ΔV_w) for the objects in our sample. The final column gives the estimated radii of the [O III] outflow regions. For most of the objects these have been estimated by fitting a Gaussian to the core of the [O III] $\lambda\lambda 5007, 4959$ spatial profile along the slit, with the radius estimated as $R_{[\text{O III}]} = \text{FWHM}(\text{kpc})/2$. However, in the case of F13451+1232 the radius was estimated from the narrow-band images published in Batcheldor et al. (2007).

Object	FWHM_w	ΔV_w	$R_{[\text{O III}]}$
IRAS	(km s^{-1})	(km s^{-1})	(kpc)
(1)	(2)	(3)	(4)
F00188–0856	904 ± 79	-253 ± 36	2.2
F01004–2237	1377 ± 197	-778 ± 112	3.5
F12072–0444	886 ± 100	-351 ± 38	2.0
F13305–1739	1368 ± 49	-92 ± 5	3.2
F13428+5608	1368 ± 66	$+14 \pm 11$	1.5
F13451+1232	1454 ± 145	-860 ± 86	0.2
F14394+5332	989 ± 28	-942 ± 26	1.4
F15130–1958	1336 ± 402	-606 ± 186	1.7
F15462–0450	1426 ± 40	-822 ± 25	1.4
F16156+0146	1099 ± 97	-262 ± 23	2.4
F17044+6720	1765 ± 103	-553 ± 65	3.1
F17179+5444	941 ± 116	-74 ± 16	1.6
F23060+0505	797 ± 38	-333 ± 18	1.8
F23233+2817	1317 ± 58	-522 ± 39	1.4
F23327+2913	804 ± 14	-94 ± 4	1.5
F23389+0300	2223 ± 30	$+47 \pm 13$	1.4

types of active galaxies. Indeed, many ULIRGs show compelling evidence for AGN activity at mid-IR wavelengths (Veilleux et al. 2009), but no sign of such activity at optical wavelengths.

Unfortunately, estimating the reddening is challenging based on our existing data. $\text{H}\alpha$ is in a blend, and there are potentially degeneracies involved in the fits that may affect the accuracy of the line ratio measurements, especially in cases with highly complex, multiple-component line profiles. Nonetheless, we used the $\text{H}\alpha/\text{H}\beta$ ratios in Table 3 to calculate a ‘crude’ estimate of the de-reddened [O III] luminosities. We then used these de-reddened luminosities to reproduce Fig. 2 and obtained identical results, i.e. no trends and correlations are found. Furthermore, we carried out the same exercise but using the [O IV] 25.89 luminosities from Veilleux et al. (2009), which are a more reliable AGN luminosity indicator and are available for nine ULIRGs in our sample. The results obtained are identical to those of the previous attempt, i.e. no trends and correlations are found.

3.4 The spatial scales of the kinematically disturbed regions

Our analysis of the emission line profiles has concentrated on spatially integrated, 5 kpc diameter aperture, data. However, in order to properly quantify the outflows it is important to attempt to estimate their spatial extents within the apertures. Spatially resolved, kpc-scale emission line outflows are found in many Seyfert galaxies, and directly detected in one low- z Sy-ULIRG (Mrk 231; see Rupke & Veilleux 2011). Moreover, Alexander et al. (2010) and Harrison et al. (2012) have recently found evidence for outflows on a scale of 4–15 kpc in a sample of high- z ULIRGs. In contrast, *Hubble Space Telescope* (HST) emission line imaging of the outflows in two radio-loud ULIRGs – PKS 1345+12 and PKS 1549–79 – shows that they are significantly more compact, with radial extents of only ~ 100 – 200 pc (Batcheldor et al. 2007). Therefore, the radial

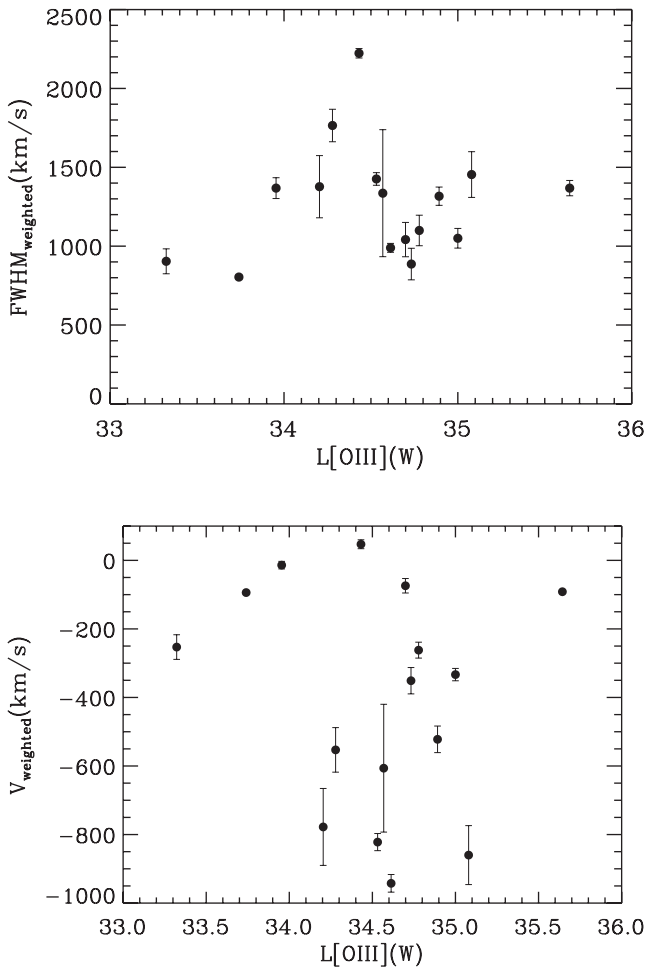


Figure 2. Flux-weighted mean FWHM (FWHM_w) and shifts (ΔV_w) plotted against the $[\text{O III}] \lambda 5007$ luminosities ($L_{[\text{O III}]}$) of the sources.

extents of the AGN-induced outflows in the Sy-ULIRGs in the local Universe are highly uncertain.

Based on visual inspection of our 2D long-slit data, we find that the dominant broad/intermediate kinematic components are generally confined to the central few pixels – on a similar scale to the seeing FWHM estimated by the DIMM seeing monitor at the time of the observations. More quantitatively, we have extracted the continuum-subtracted spatial profiles of the $[\text{O III}]$ emission from the 2D frames and fitted Gaussians to the central cores of the profiles. We show the results in column 4 of Table 4, quantified as $\text{FWHM}/2$ in units of kpc. We find that the $[\text{O III}]$ FWHM estimates are comparable with the DIMM seeing estimates at the times of the observations for ~ 56 per cent of the objects in our sample. Moreover, in some objects the spatial profiles may be dominated by spatially resolved narrow components. Therefore, in most cases the numbers presented in column 4 of Table 4 are likely to represent upper limits on the true spatial extents of the near-nuclear warm outflows.

Overall, based on our measurements of the spatial profiles of the $[\text{O III}]$ emission in our sample of Sy-ULIRGs, and the direct *HST* imaging estimates of the scales of the outflow regions in PKS 1345+12 and PKS 1549–79 (Batcheldor et al. 2007), it is likely that the radial extents of the near-nuclear outflows fall in the range $0.1 < r < 3.5$ kpc.

4 DISCUSSION

4.1 Are the outflows jet-driven?

Spoon & Holt (2009) found evidence for a correlation between the width of the mid-IR $[\text{Ne III}]$ line at $15.56 \mu\text{m}$ and the 1.4 GHz radio luminosity ($L_{1.4\text{GHz}}$), based on *Spitzer* IRS observations of a combined sample of ULIRGs and local Seyfert galaxies. The correlation is in the sense that some of the objects with the highest radio powers have the most extreme emission line kinematics, suggesting that the outflows might be jet-driven. Further evidence for jet-driven outflows in ULIRGs is provided by *HST* images which show that the outflow regions have similar scales to the relativistic radio jets in two of the most extreme radio-loud ULIRGs with high-velocity outflows (Batcheldor et al. 2007).

In Fig. 3, we show the weighted mean velocity shifts and FWHM plotted against the radio powers listed in column 7 of Table 1. Note that an important caveat with interpreting this plot in terms of jet-driven outflows is that the radio emission does not necessarily have an AGN origin in the ULIRGs, but may instead be associated with

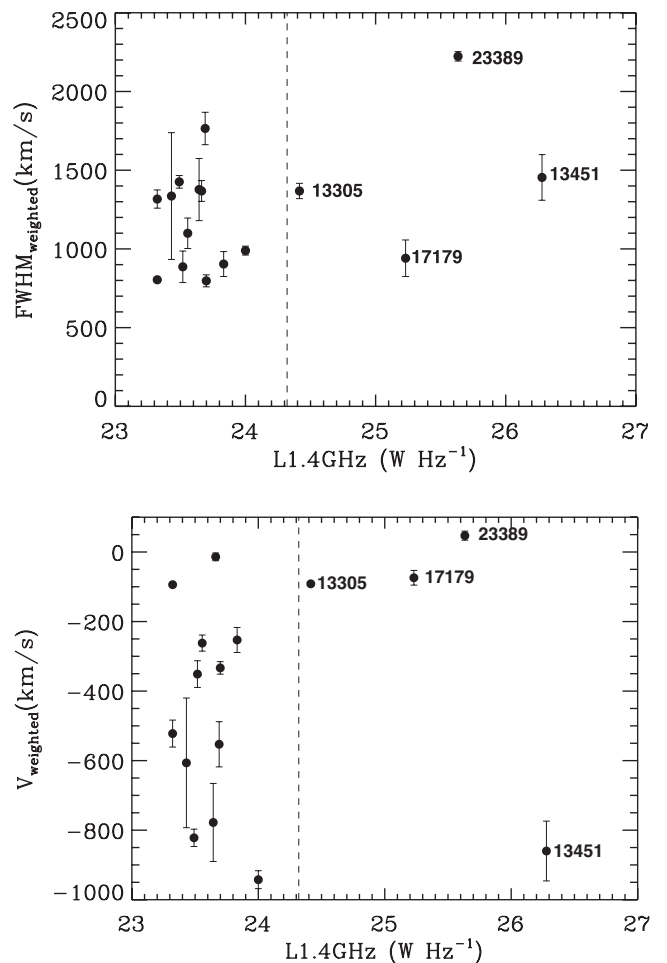


Figure 3. Same as Fig. 2 but with the 1.4 GHz monochromatic radio luminosities ($L_{1.4\text{GHz}}$). The dashed line indicates the maximum 1.4 GHz luminosity for the galaxies in our sample calculated using their L_{IR} along with the Condon et al. (1991b) IR–radio luminosity relation for starburst galaxies. Four objects show an excess of radio emission for their corresponding L_{IR} , which reveals the presence of a strong AGN component. These objects are indicated in the figure using the first five digits of their designation in the *IRAS* FSC Database.

the prodigious starburst activity. The vertical dashed line in Fig. 3 show the maximum radio power expected for the starburst-related radio emission in the Sy-ULIRGs, as predicted on from their measured infrared luminosities and the well-known correlation between radio power and infrared luminosity for starburst galaxies (Condon, Anderson & Helou 1991b). From this, it is clear that only four of the Sy-ULIRGs – F13305–1739, F13451+1232, F17179+5444 and F23389+03000 – can be considered to have genuinely radio-loud AGN with $L_{1.4\text{GHz}} > 10^{24.3} \text{ W Hz}^{-1}$.

On the basis of Fig. 3 there is no evidence for a strong correlation between radio power and emission line kinematics. Although it is certainly true that the two most radio-powerful objects in our sample – F13451+1232 and F23389+03000 – also display some of the most extreme emission line kinematics, the other two radio-loud Sy-ULIRGs show relatively quiescent kinematics. Moreover, the radio-quiet majority of objects in our sample ($L_{1.4\text{GHz}} \lesssim 10^{24} \text{ W Hz}^{-1}$) encompass the same range of kinematic disturbance as the radio-loud objects, and some radio-quiet objects show emission line kinematics as extreme as those found in the radio-loud objects, with [O III] emission line profiles dominated by broad, shifted components (e.g. F01004–2237, F14394+5332, F15130–1958, F15462–0450). Therefore, we argue that while the emission line outflows *can* be driven by the jets in *some* Sy-ULIRGs, especially in cases where powerful relativistic jets have the same spatial scales as the emission line structures (e.g. F13451+1232; Holt et al. 2003; Batcheldor et al. 2007); in most Sy-ULIRGs there is no clear evidence for such jet-driven outflows.

4.2 Ionization mechanisms

4.2.1 AGN and starburst photoionization

It is well known that starburst and AGN activity can co-exist in the nuclear regions of ULIRGs, both energy sources potentially contributing to the ionization the surrounding gas (e.g. Genzel et al. 1998; Armus et al. 2007; Farrah et al. 2007; Veilleux et al. 2009). Therefore, it is interesting to determine whether there is a correlation between the emission line kinematics and the nature of the ionizing source(s).

Fig. 4 shows the standard, optical BPT diagnostic line ratio diagrams (Baldwin, Phillips & Terlevich 1981). The lines drawn in the diagrams correspond to the optical classification scheme of Kewley et al. (2006). Overplotted on the figure are the results from our kinematic study. Blue squares, green triangles and red circles correspond to the narrow, intermediate and broad components, respectively. The error bars have been calculated by combining the 5 per cent uncertainty of the relative flux calibration in quadrature with the uncertainty associated with the model fits.

It is notable that the line ratios obtained for most, if not all, the ULIRGs in our sample are consistent with an Sy2 classification. However, the figure demonstrates a clear trend with emission line kinematics: whereas the line ratios for the broad components (red circles) in most cases fall squarely in Seyfert part of the diagram, suggesting AGN photoionization as the dominant ionization mechanism, the line ratios for the narrow components (blue squares) measured in many objects fall in, or close to, the transition zone between H II region and Seyfert classifications – more consistent with a combination of the AGN and stellar photoionization; the ratios measured for the intermediate components (green triangles) tend to fall in between those of the narrow and the broad.

We emphasize that the trends in the emission line ratios with line width do not necessarily provide evidence for an ionization

stratification in the AGN outflow regions themselves. Rather, they are naturally explained in terms of the varying contribution of the starburst activity to the ionization of the gas associated with each of the different kinematic components. For example, it is likely that starburst activity plays an important role in ionizing the gas associated with the narrow components in many of the objects. The importance of the starburst activity as an ionizing source gradually decreases for the intermediate component. Finally, in the case of the broadest kinematic component, AGN activity is the dominant source of ionization. Note that the association between the ionization state of the gas and the line width provides further evidence that the broader (generally blueshifted) components are driven by the AGN rather than by the starburst components.

With the aim of better understanding the nature of ionization mechanisms responsible for the measured line ratios, Fig. 4 also shows the Groves et al. (2004a) dusty, radiation pressure-dominated photoionization models for NLR in AGN. For these models, we assume a hydrogen density $n_{\text{H}} = 1000 \text{ cm}^{-3}$ [the only hydrogen density used in the Groves et al. (2004a)] and twice solar abundance ($2 Z_{\odot}$). This later value was found by Groves, Dopita & Sutherland (2004b) to provide a better match to the line ratios measured in Seyfert NLR (Groves et al. 2004b). A grid of models for various values of the ionizing parameter ($U_0 = 0, -1, -2, -3, -4$) and ionizing continuum SED power-law indices ($F_{\nu} \propto \nu^{\alpha}$, $\alpha = -1.2, -1.4, -1.7, -2.0$) is shown in the figure.

At first sight it is apparent that, with few exceptions, the line ratios of the intermediate and the broad kinematic components fall within the grids of models in the case of the diagram involving [O I]/H α . However, these models fail to reproduce most of the line ratios for such components in the case of the [N II]/H α diagram (and to a lesser extent in the case of the [S II]/H α diagram). A possible explanation for this finding is that the emission-line regions are more metal rich than we have assumed. In this context, Fig. 5 shows the [O III] 5007/H β versus [N II] 6583/H α diagram assuming $n_{\text{H}} = 1000 \text{ cm}^{-3}$ and $4 Z_{\odot}$ (the other two diagrams remain relatively unchanged after increasing the metallicity and therefore are not shown in the figure). It is clear from the figure that a $4 Z_{\odot}$ abundance certainly improves the match between the models and our data. Therefore, the line ratios derived for the Sy-ULIRGs in our sample are consistent with gas of supersolar abundances that has been photoionized by a combination of starburst and AGN components, with the AGN photoionization dominating for the broad/shifted kinematic components.

4.2.2 Shock ionization

As well as photoionization by AGN and starburst activity, it is possible that line ratios plotted in Fig. 4 can also be explained in terms of ionization by fast radiative shocks (Dopita & Sutherland 1995, 1996; Groves et al. 2004a; Allen et al. 2008). The shock models predict a series of line ratios for a range of magnetic field (B), electron densities (n_e), abundances and shock velocities (v_s). In addition, the predicted line ratios depend on the geometry of the shock, i.e. the presence of a photoionized precursor of the shock (see Allen et al. 2008 for a detail discussion).

Fig. 6 shows the Allen et al. (2008) models with solar metallicity (Z_{\odot}) and a pre-shock density of 100 cm^{-3} . Based on the results in the previous section, it might be more appropriate to use models with higher metallicities. However, the highest metallicity used in Allen et al. (2008) is $2 Z_{\odot}$, and for this value only n_e values of 1 and 1000 are considered. Therefore, we

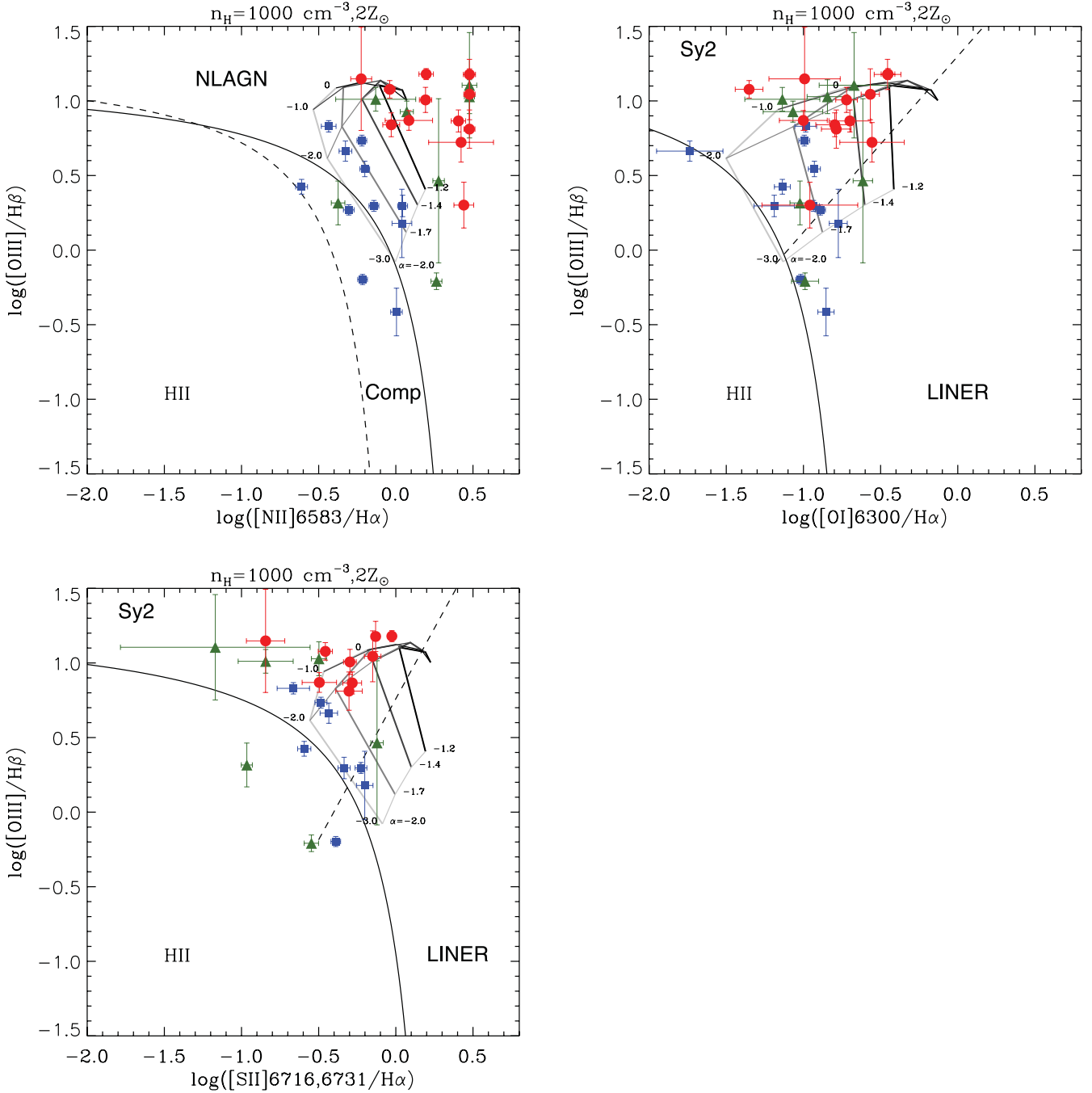


Figure 4. Standard optical diagnostic diagrams showing the classification scheme of Kewley et al. (2006). The solid curves are the theoretical ‘maximum starburst line’ derived by Kewley et al. (2001) as an upper limit for star-forming galaxies and the empirical boundary lines between Seyfert 2 galaxies and LINERs. The dashed curve on the [NII] diagram represents the Kauffmann et al. (2003) semi-empirical lower boundary for the star-forming galaxies. The Groves, Dopita & Sutherland (2004a) grids of dusty, radiation pressure-dominated models are also plotted in the Figure. These grids have been generated assuming twice solar metallicity ($2 Z_\odot$) and hydrogen density of $n_H = 1000 \text{ cm}^{-3}$. Gridlines corresponding to five values of ionizing parameter ($U_0 = 0, -1, -2, -3, -4$) and four values of power-law index ($F_\nu \propto \nu^\alpha$, $\alpha = -1.2, -1.4, -1.7, -2.0$) are shown in the figure. To help the reader follow the gridlines these are grey-coded from ‘light grey’ to black, with light grey and black corresponding to the lowest and highest values of U_0 and α , respectively. Overplotted on the diagrams are the results of our kinematic study. The blue squares represent the line ratios corresponding to the narrow components, the green triangles correspond to the intermediate component and the red circles represent the broadest kinematic component.

decided to use Z_\odot , models since they sample the parameter space better.

One of the largest uncertainties in these models is the pre-shock density. Assuming that we measure the density of the compressed post-shock gas in the kinematically disturbed emission line compo-

nents that we detect in the ULIRGs in our sample, and the measured electron densities of these components are 1000 cm^{-3} (see section 4.3), then the pre-shock densities could be as low as $10\text{--}100 \text{ cm}^{-3}$, since the compression factor in the cooled, post-shock gas can be high ($\sim 10\text{--}100$; see Dopita & Sutherland 1995). Therefore, we

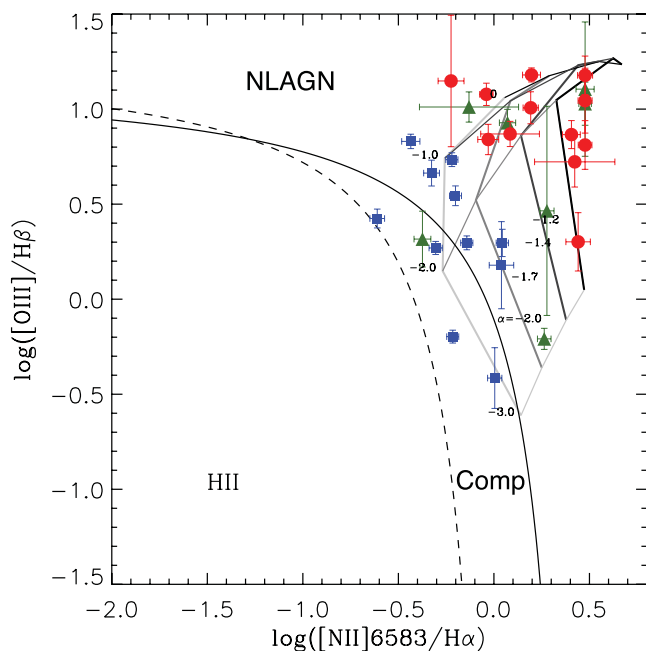


Figure 5. Same as Fig. 4 but only for the [N II] 6583/H α diagram and for $4 Z_{\odot}$. The other two diagrams remain relatively unchanged by the increase in metallicity and therefore are not shown in the figure.

have assumed a pre-shock density of 100 cm^{-3} . Finally, Dopita & Sutherland (1995) and Allen et al. (2008) found that the shock+precursor models produce a better fit to the line ratios measured for their samples of Sy2 and luminous IR galaxies. For this reason, we decided to use such models for the work presented in this section. The potential effects of changing these assumptions is discussed later in the section. The gridlines correspond to three values of B from 1–100 μG (1, 10 and 100 μG), which are appropriate for starburst galaxies (Thompson et al. 2006), and nine values of v_s (200, 300, 400, 500, 600, 700, 800, 900 and 1000 km s^{-1}). The direction in which B increases is indicated in the figure with an arrow, while v_s increases from bottom to top with three values (200, 400 and 1000 km s^{-1}) indicated in the figure.

As seen in the figure, most of the measured line ratio values do not fall within the region covered by the grids of shock models; the lack of agreement between the models and the data is particularly apparent in the diagnostic diagram that involves the [O I]/H α ratio. However, the models have a relatively large number of free parameters (B , v_s , n_e and abundance) plus the additional possibility of including or otherwise the shock precursor component. Therefore, it is possible to cover wide ranges of line ratio values using different assumptions. For example, using twice solar abundance models with a pre-shock density of 1000 cm^{-3} instead of 100 cm^{-3} substantially extends the gridlines in the three diagrams (see Allen et al. 2008 for details), providing a better match to the measured line ratios. We note that the line ratio values measured for some of the broad kinematic components fall outside the Allen et al. (2008) grids of shock models, or are only reproduced by the most extreme set of parameter values (e.g. $n_e = 1000 \text{ cm}^{-3}$ and $B = 1000 \mu\text{G}$).

Overall, we find that the line ratios measured for our sample of Sy-ULIRGs are, in general, better reproduced by photoionization models that include a combination AGN and starburst photoionization and in which the emitting gas is highly enriched in metals. However, as pointed out by Dopita and collaborators (e.g. Dopita

& Sutherland 1995, 1996; Groves et al. 2004b; Allen et al. 2008), it is not always possible to decisively distinguish between shock ionization and AGN photoionization using only the stronger optical emission lines included in the diagnostic plots of Fig. 6.

4.3 Physical conditions and reddening

Potentially, further clues to the nature of the emission line outflows may be obtained by considering the reddening and densities of the emission line components. For example, Holt et al. (2003, 2011) found evidence that the broadest and most highly shifted emission line components in F13451+1232 (PKS 1345+12) are also the most highly reddened, suggesting that the outflows are stratified and decelerating, with the fastest components associated with most highly reddened regions closest to the driving AGN. Similarly, if the most highly disturbed kinematic components are truly associated with the regions closest to the AGN, we might expect them to show evidence for higher densities than the less kinematically disturbed components.

On the outset, it is important to emphasize that estimating the reddening and densities for the broad, shifted kinematic components is challenging based on our existing data, because some of the key emission lines (e.g. H α , [S II] $\lambda\lambda 6717, 6731$) are in blends, and there are potentially degeneracies involved in the fits that may affect the accuracy of the line ratio measurements, especially in cases with highly complex, multiple-component line profiles (see discussion in Section 3.1).

To search for reddening gradients, we use the H α /H β ratio, which, for typical NLR conditions and AGN photoionizing continuum shapes, is expected to have a value in the range $2.8 < \text{H}\alpha/\text{H}\beta < 3.1$ in the absence of reddening (Gaskell & Ferland 1984; Osterbrock 1989). Column 9 in Table 3 gives the H α /H β line ratio values for the various kinematic components of the galaxies in our sample. At first sight, the modelling results appear to show evidence for a trend of increasing reddening with line width in four of the ULIRG Seyferts (F13451+1332, F14349+5332, F17179+544, F23060+0505). However, two objects apparently show the reverse trend (F00188–0856, F15462–0450), and in most cases there is no clear trend. Clearly, given the large uncertainties in the measured ratios – to some extent reflecting the degeneracies in the fits – the results are inconclusive.

The results are no more decisive when it comes to estimating the densities using the [S II] (6717/6731) ratio (see the discussion of individual objects in the Appendix). While it has proved possible to derive accurate densities for the narrow emission line components in some objects (typical electron densities: $2.4 \times 10^2 < n_e < 3.6 \times 10^3 \text{ cm}^{-3}$), we have failed to measure accurate densities for the broader emission line components in any object. However, in the cases of F13305–1739, F13428+5608, F15462–0405 and F23233+2817, it has been possible to derive lower limits on the electron densities of the broad components of $9 \times 10^2, 6 \times 10^2, 4 \times 10^2$ and $4 \times 10^2 \text{ cm}^{-3}$, respectively.

4.4 Mass outflow rates and energetics

AGN feedback is now routinely incorporated into numerical simulations of the hierarchical growth of galaxies through major galaxy mergers. To reproduce the correlations between the masses of the black holes and the bulge properties (e.g. Silk & Rees 1998; di Matteo et al. 2005) some of these models require that a relatively large fraction of the available accretion power of the quasars is thermally coupled to the circumnuclear interstellar medium

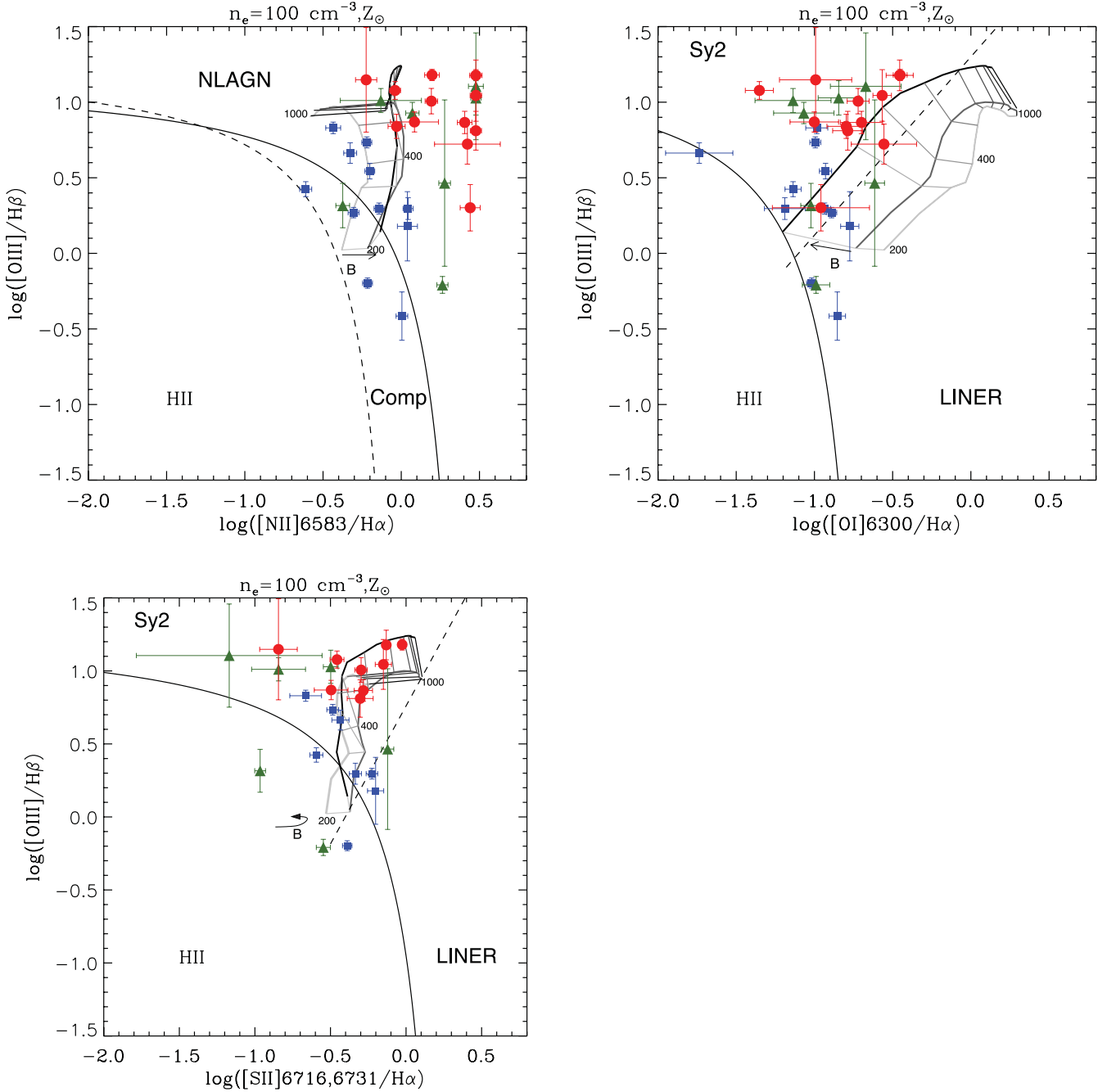


Figure 6. Same as Fig. 4 but showing the Allen et al. (2008) grids of shock-ionization models. These grids have been generated assuming a shock+precursor model with solar metallicity and pre-shock density of $n_e = 100 \text{ cm}^{-3}$. Gridlines corresponding to three values of magnetic field ($B = 1, 10$ and $100 \mu\text{G}$) and nine shock velocity values ($v_s = 200, 300, 400, 500, 600, 700, 800, 900$ and 1000 km s^{-1}) are shown in the figure. The increasing direction of B is indicated with an arrow. In the case of the $[\text{S II}]/\text{H}\alpha$ diagram, B increases first to the right and then to left which is indicated with a curved arrow. v_s increases always from bottom to top with three values ($200, 400$ and 1000 km s^{-1}) indicated in the figure. As in the case of Fig. 4, the gridlines are grey-coded from ‘light grey’ to black, with light grey and black corresponding to the lowest and highest values of B and v_s , respectively.

(~ 5 – 10 per cent; e.g. Fabian 1999; di Matteo et al. 2005, but see Hopkins et al. 2010).

As described in the introduction, ULIRGs represent just the situation modelled in many of the merger simulations that include AGN feedback. In order to investigate whether our observational results are consistent with those of the merger simulations, it is important to quantify the mass outflow rates and the kinetic powers of the outflows.

For a spherical outflow, the mass of the ionized gas in the outflow is given by

$$M = n_e m_p V \epsilon, \quad (3)$$

where n_e is the electron density, m_p the mass of the proton, V is the total volume and ϵ is the gas filling factor (Osterbrock & Ferland 2006). Therefore, for a steady state outflow, the mass

outflow rate is

$$\dot{M} = n_e m_p v_{\text{out}} A \epsilon, \quad (4)$$

where v_{out} is the velocity of the outflow and A is the surface area of the outflowing region. Also, the filling factor ϵ is related to the $H\beta$ luminosity, the electron density n_e and the emitting volume V by

$$\epsilon = \frac{L(H\beta)}{\alpha_{H\beta}^{\text{eff}} h \nu_{H\beta} n_e^2 V}; \quad (5)$$

hence, the mass outflow rate is related to the $H\beta$ luminosity by

$$\dot{M} = \frac{L(H\beta) m_p v_{\text{out}} A}{\alpha_{H\beta}^{\text{eff}} h \nu_{H\beta} n_e V}. \quad (6)$$

For a spherical outflow geometry this reduces to

$$\dot{M} = \frac{3L(H\beta) m_p v_{\text{out}}}{\alpha_{H\beta}^{\text{eff}} h \nu_{H\beta} n_e r}, \quad (7)$$

where r is the radius of the spherical volume. In addition, the kinetic power of the outflow (\dot{E}) is related to the velocity dispersion ($\sigma \approx \text{FWHM}/2.355$), mass outflow rate and outflow velocity by

$$\dot{E} = \frac{\dot{M}}{2} (v_{\text{out}}^2 + 3\sigma^2). \quad (8)$$

The main uncertainty in calculating the mass outflow rates, and hence the kinetic powers of the outflows, is related to the electron density. Unfortunately, as we saw in the previous section, due to degeneracies in the fits to the [S II] lines, the densities are relatively unconstrained for the broad, shifted components in most of the objects in our sample. In this case, the densities could range from the relatively low values typically determined for the spatially resolved NLR in some objects ($n_e \sim 100 \text{ cm}^{-3}$; Taylor et al. 2003, Robinson et al. 2000) up to the much higher densities directly measured for the outflow components in F13451+1232 using the transauroral line ratios ($2 \times 10^4 < n_e < 5 \times 10^5 \text{ cm}^{-3}$; Holt et al. 2011) – a range of almost four orders of magnitude. Other sources of uncertainty include the $H\beta$ luminosities, which are affected by uncertain reddening corrections (see the previous section), and the uncertain radii (r) of the outflows (see Section 3.4). Each of these adds at least a further order of magnitude uncertainty when calculating the properties of the outflows.

In order to gain an impression of the range of possible mass outflow rates and kinetic powers for the warm outflows in the Sy-ULIRGs, we have calculated upper and lower limits on these quantities, based on the emission line kinematics from Table 2 and assuming that $\Delta V = V_{\text{out}}$ for each of the kinematic components. To derive the lower limits, we have used the high density estimated by Holt et al. (2011) for the broadest component in F13451+1232 ($n_e = 5 \times 10^5 \text{ cm}^{-3}$), the upper radius limits given in column 4 in Table 4, and $H\beta$ luminosities that have not been corrected for reddening; whereas for the upper limits we have assumed a density of 100 cm^{-3} , a radius of 0.1 kpc and the reddening-corrected $H\beta$ luminosities. Note that low densities, small radii and high $H\beta$ luminosities favour highly massive and energetic outflows. In the case of F13451+1232, the density, reddening-corrected $H\beta$ luminosity and radius of the outflow are known relatively accurately from the studies of Batcheldor et al. (2007) and Holt et al. (2011); for this object, we have used the results from the latter studies to calculate the outflow properties.

As expected, with the exception of F13451+1232, the estimates of the outflow properties are highly uncertain, and encompass several orders of magnitude in both mass outflow rate and kinematic power for individual kinematic components in individual

objects. Across our sample we find upper limiting mass outflow rates in the range $1 < \dot{M} < 1.5 \times 10^3 M_{\odot} \text{ yr}^{-1}$ and upper limiting kinetic powers in the range $5 \times 10^{41} < \dot{E} < 2 \times 10^{45} \text{ erg s}^{-1}$. To put these numbers into context, we can compare them with the bolometric radiative powers of the AGN, which provide an indication of the available accretion power of the material being accreted on to the supermassive black holes. We calculate the bolometric luminosities of the individual AGN by multiplying the infrared luminosities from Table 1 by the fractional contributions of the AGN to the infrared light from mid-IR spectroscopic study of the QUEST sample by Veilleux et al. (2009),⁵ obtaining values in the range $2 \times 10^{45} < L_{\text{BOL}}^{\text{AGN}} < 6 \times 10^{45} \text{ erg s}^{-1}$. Therefore, considering the extreme high end of the upper limits, the warm outflows in Sy-ULIRGs can have kinetic powers that are comparable with the radiative luminosities of the AGN. However, at the lower end of the range of upper limits – including F13451+1232 with its more precise \dot{E} estimates (see Holt et al. 2011) – the kinetic powers of the outflows are only a small fraction of the bolometric luminosities (<0.5 per cent) – well below the levels required by some of the models (e.g. Silk & Rees 1998; Fabian 1999; di Matteo et al. 2005), but perhaps consistent with the two-stage feedback mechanism described by Hopkins & Elvis (2010).

The discrepancy with the models grows even stronger if we consider the range of lower limiting mass outflow rates and kinetic powers encompassed by our sample: $4 \times 10^{-5} < \dot{M} < 4 \times 10^{-3} M_{\odot} \text{ yr}^{-1}$ and $4 \times 10^{35} < \dot{E} < 2 \times 10^{39} \text{ erg s}^{-1}$. If these values proved correct, the AGN outflows would have a negligible impact on the overall evolution of their host galaxies.

4.5 Comparison with the emission line kinematics of other samples of Seyfert galaxies and other types of AGNs

The hydrodynamical models predict that the AGN-induced outflows should be particularly strong in the final stages of the type of major, gas-rich mergers represented by ULIRGs. Therefore, it is interesting to consider whether the degree of kinematic disturbance in ULIRGs with optical Seyfert nuclei is unusual compared with samples of non-ULIRG AGN.

4.5.1 Comparison with previous kinematic studies of the NLR in Seyfert galaxies

For our first comparison, we use the Heckman et al. (1981), Whittle (1985), Veilleux (1991a) and Nelson & Whittle (1995) studies of the narrow emission line kinematics in samples of local Seyfert and radio galaxies. In general, although these samples are likely to be representative of nearby Seyfert galaxies, their selection criteria are not well defined. The exception is the Veilleux (1991a) sample, for which the objects have $\delta \gtrsim -25^\circ$ and $F([\text{O III}]) \lesssim 5007 \geq 1 \times 10^{-13} \text{ erg s}^{-1} \text{ cm}^{-2}$ (see Veilleux 1991a for a discussion of the potential biases due to their selection criteria). The general properties of these samples are compared with those of the Sy-ULIRGs in Table 5. We note that, although these samples encompass a similar range of [O III] emission line luminosity to our Sy-ULIRG sample, they tend to contain a higher proportion of lower luminosity objects.

⁵ Note that for objects in our sample that were not included in the Veilleux et al. (2009) QUEST sample, we assume that the AGN contribute 50 per cent of the infrared light – a typical value for the QUEST sample objects.

Table 5. Details of the properties of the local Seyfert comparison samples. The [O III] $\lambda 5007$ flux values for the sources within these comparison samples have been taken from Dahari & De Robertis (1988), Gu et al. (2006), Moustakas & Kennicutt (2006), Massaro et al. (2009), Tremblay et al. (2009), González-Martín et al. (2009), LaMassa et al. (2010), Greene et al. (2010) and Rose (private communication).

Sample	Selection criteria	Redshift range	$L_{[\text{O III}]}$ range (W)	Resolution (km s ⁻¹)
Sy-ULIRGs (this paper)	$S_{60} > 1$ Jy, $L_{\text{IR}} > 10^{12} L_{\odot}$, emission line ratios	$z < 0.175$	$2 \times 10^{33} - 4 \times 10^{35}$	~ 230
Heckman et al. (1981)	Representative of local Seyferts	$z < 0.076$	$3.5 \times 10^{32} - 1.7 \times 10^{35}$	~ 130
Whittle (1985)	Representative of local Seyferts	$z < 0.066$	$2.3 \times 10^{32} - 3.3 \times 10^{35}$	40–80
Veilleux (1991a)	$F_{[\text{O III}]} \geq 1 \times 10^{-13}$ erg s ⁻¹ cm ⁻²	$z < 0.028$	$5.8 \times 10^{32} - 1.8 \times 10^{35}$	~ 10
Nelson & Whittle (1995)	Representative of local Seyferts	$z < 0.043$	$2.1 \times 10^{31} - 1.7 \times 10^{35}$	80–230

The previous studies of nearby Seyfert galaxies investigated the kinematics of the NLR using a parameter scheme based on cuts across the profiles at different heights. We will concentrate here in the so-called asymmetry ($A/20$) and kurtosis ($K1$) parameters as defined by Heckman et al. (1981) and Whittle (1985) as follows:

$$A/20 = \frac{WL20 - WR20}{WL20 + WR20}, \quad (9)$$

where $WL20$ and $WR20$ are the widths to the right and left of the line centre defined at the 80 per cent intensity level ($C80$), and

$$K1 = 1.524 \times \frac{W50}{W20}, \quad (10)$$

where $W50$ and $W20$ are the widths at 50 and 20 per cent intensity level (i.e. $W50 \equiv \text{FWHM}$ of the line). The kurtosis $K1$ parameter is defined such that for a Gaussian $K1 = 1.0$. Line profiles with $K1$ values lower or higher than 1 are called platykurtic ('peaky') or leptokurtic ('stubby'), respectively.

Table 6 shows the values of $A/20$, $K1$, $W20$ and $W50$ for the Sy-ULIRGs in our sample. Since the previous studies considered here concentrate mostly on the [O III] $\lambda 5007$ emission line, the values in the table have been estimated using that line. When more than one kinematic narrow component is clearly visible in the emission line profile of a source (e.g. IRAS F14394+5332), the wavelength of peak of the intensity (i.e. $C80$) is defined using the kinematic component at rest frame. In addition, in the case of the Sy1 IRAS F15130–1958, we used our modelling results to subtract the Fe II emission prior to calculating the parameters.

Fig. 7 shows $A/20$ plotted against $K1$ and $W20$. Nelson & Whittle (1995) do not provide the centre at 20 per cent intensity level in their paper and therefore it is not possible to estimate the $A/20$ parameter for the objects in their sample. At first sight, the figure shows the well-known tendency for the [O III] $\lambda 5007$ in Seyfert galaxies to have blueward asymmetries (Heckman et al. 1981; Whittle et al. 1988). In addition, the upper panel of the figure shows that, although the values of the different parameters found for the Sy-ULIRGs are consistent with the main body of points for the four comparison samples, a significant proportion (at least 5 of 17, 30 per cent) are outliers in these plots. Moreover, the lower panel in Fig. 7 shows that Sy-ULIRGs have, in general, broader emission lines than the objects in the comparison samples. It is also apparent in the figure that all three of the objects with the most asymmetric profiles are Sy-ULIRGs.

Table 6. The emission line parameters for the Sy-ULIRGs in our sample. Column (1): galaxy name. Column (2): width at 20 per cent of the peak intensity level. Column (3): width at 50 per cent of the peak intensity level. Column (4): the asymmetry $A/20$. Column (5): the kurtosis parameter $K1$. All these parameter values have been quadratically corrected for the instrumental profile.

Object	W20 (km s ⁻¹)	W50 (km s ⁻¹)	$A/20$	$K1$
(1)	(2)	(3)	(4)	(5)
F00188–0856	1207 ± 32	509 ± 56	0.24 ± 0.05	0.64 ± 0.10
F01004–2237	1779 ± 30	249 ± 42	0.71 ± 0.03	0.21 ± 0.09
F12072–0444	1002 ± 30	544 ± 36	0.31 ± 0.04	0.83 ± 0.14
F12112+0305	743 ± 18	388 ± 36	−0.20 ± 0.06	0.79 ± 0.09
F13305–1739	1786 ± 31	1072 ± 29	0.11 ± 0.02	0.91 ± 0.05
F13428+5608	949 ± 36	540 ± 36	0.00 ± 0.04	0.88 ± 0.05
F13451+1232	706 ± 31	1553 ± 36	0.34 ± 0.02	0.68 ± 0.03
F14394+5332	2091 ± 42	1488 ± 30	0.65 ± 0.04	1.08 ± 0.05
F15130–1958	2029 ± 30	1156 ± 42	0.28 ± 0.05	0.87 ± 0.14
F15462-0450	2208 ± 46	1659 ± 40	0.68 ± 0.05	1.14 ± 0.09
F16156+0146	989 ± 29	297 ± 30	0.36 ± 0.03	0.46 ± 0.13
F17044+6720	640 ± 21	296 ± 29	0.04 ± 0.03	0.70 ± 0.03
F17179+5444	1202 ± 29	645 ± 29	0.07 ± 0.03	0.82 ± 0.06
F23060+0505	1315 ± 32	721 ± 30	0.38 ± 0.03	0.83 ± 0.10
F23233+2817	1459 ± 34	834 ± 29	0.31 ± 0.05	0.87 ± 0.14
F23327+2913	1151 ± 40	639 ± 40	0.27 ± 0.02	0.84 ± 0.11
F23389+0300	2294 ± 36	571 ± 29	0.07 ± 0.01	0.38 ± 0.05

To investigate the possible differences between non-ULIRG Seyfert galaxies and Sy-ULIRGs, Table 7 shows the mean values and estimated uncertainties for $A/20$, $K1$, $W20$ and $W50$. The results in the table provide strong evidence that, in general, the emission lines of the Sy-ULIRGs are more asymmetric than those of non-ULIRG Seyfert galaxies. Furthermore, the $W20$ values (and to a lesser extent the $W50$ values) for the Sy-ULIRGs are substantially higher than those of the objects in the comparison samples. Therefore, our results also suggest that the Sy-ULIRGs have broader emission lines compared to non-ULIRG Seyfert galaxies.

To further investigate the statistical significance of any differences between the kinematic properties of the Sy-ULIRGs and the non-ULIRG Seyferts, we have performed a variety of statistical tests. In the first instance, we used the 2D kolmogorov-Smirnov (KS) test of Peacock (1983) to investigate the significance of the differences between the positions of the Sy-ULIRGs and the comparison samples in Fig. 7. The results are shown in Table 8. We

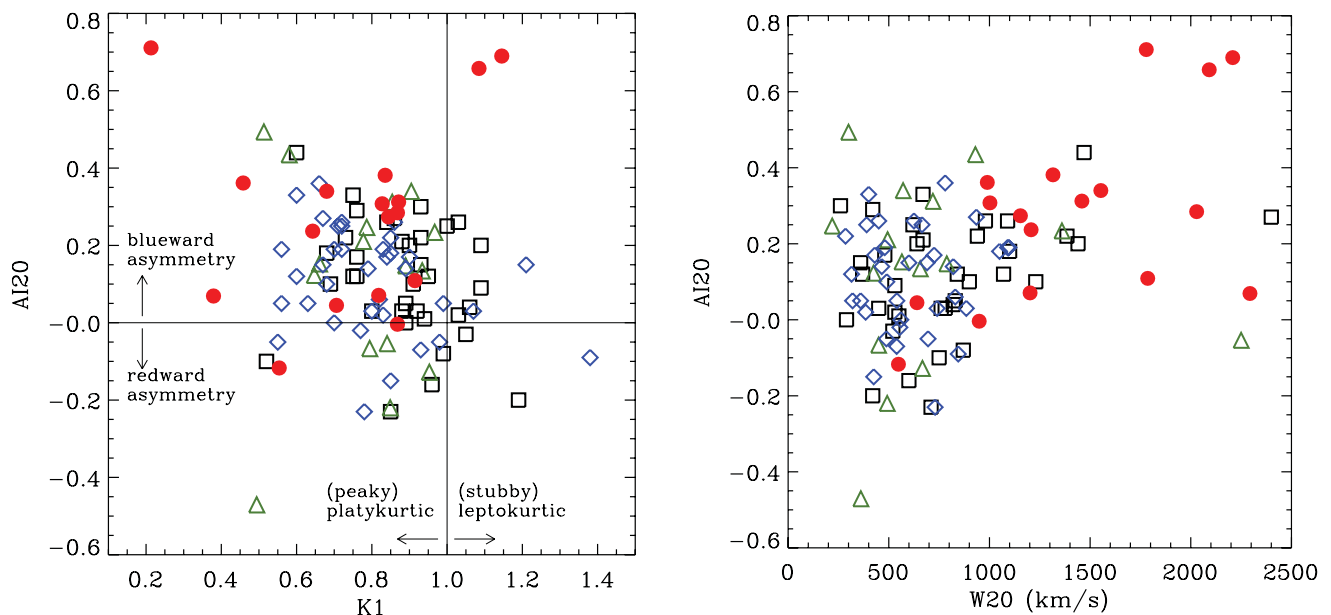


Figure 7. Left: the asymmetry $A/20$ plotted against the kurtosis parameter $K1$ for the different samples of Sy galaxies. Open black squares: Heckman et al. (1981). Open blue diamonds: Whittle (1985). Open green triangles: Veilleux (1991a). Filled red circles: our sample of Sy-ULIRGs. $A/20$ values higher (lower) than 0 indicate blueward (redward) asymmetries, while $K1$ values lower (higher) than 1 indicate ‘peaky’ (‘stubby’) profiles. For a perfectly symmetric profile $A/20 = 0$, while $K1 = 1$ for a Gaussian profile. Right: the asymmetry $A/20$ plotted against $W20$.

find that, especially considering the comparison with all the Seyfert galaxy samples combined, the differences are significant at the $\gtrsim 3\sigma$ level.⁶

We have also compared the distributions of $A/20$, $K1$, $W50$ and $W20$ separately using a 1D two sample KS test. The results are consistent with those of the 2D KS test of Peacock (1983) and are shown in Table 9. We find that, although the emission line in Sy-ULIRGs are not particularly more ‘peaky’ or ‘stubby’ than those of the comparison samples, they tend to be more asymmetric, and they are certainly broader: the difference between the $W20$ and $W50$ parameters for the Sy-ULIRGs in our sample and the objects in the comparison samples is significant at the $>3\sigma$ level.

At this stage is important to note that, while the comparison samples include a significant fraction of broad-line Seyfert 1 galaxies, our sample of Sy-ULIRGs includes only one such object. This could be a problem if the NLR kinematics depend on Seyfert type (e.g. because of orientation effects). In this context, the results of Heckman et al. (1981) show that galaxies with a significant broad-line region (BLR) component have, on average, narrower $[O\text{ III}]$ lines than those that do not have such components. However, the more comprehensive studies of Whittle (1985) and Nelson & Whittle (1995) found no evidence for differences between the line width distributions of Sy1 and Sy2 galaxies of similar $[O\text{ III}]$ luminosity and bulge properties. To explore any potential biases due to the different proportions of Sy1 objects in the Sy-ULIRG and comparison samples, we have repeated the analysis described above but this time including only in those objects classified as Sy2 for each individual sample. The results are consistent with the previous results described in this section, although with slightly less significance in the case of the $A/20$ parameter.

⁶ Those objects included in more than one of the comparison samples are only considered once for this comparison. In particular, we used the set of parameter values that are derived with the data set for which the spectral resolution most resembles the spectral resolution of our spectroscopic data.

To summarize, these results provide evidence that the emission line kinematics of the Sy-ULIRGs are more highly disturbed than those of the non-ULIRGs Seyferts in the comparison samples. Indeed, three of the objects in our sample show more extreme emission line kinematics than *any* of Seyfert galaxies in the comparison samples. However, we emphasize that the size of our Sy-ULIRGs sample is relatively small. Therefore, the results from the KS test must be interpreted carefully. Observations of larger samples of Sy-ULIRGs will be required to put this result on a firmer statistical footing.

4.5.2 Comparison with the emission line kinematics of other types of AGN

Whittle (1985) found evidence – albeit weak – for correlations between the emission line kinematics and the luminosities of the associated AGN. Given that the Seyfert galaxy comparison samples considered in the previous section contain a higher proportion of objects with low $[O\text{ III}]$ luminosities than our Sy-ULIRG sample, it is therefore important to make comparisons with samples that include higher luminosity objects. For this purpose we use the following three AGN samples: the Palomar–Green (PG) sample of nearby quasars [Boroson et al. 1982; Rose et al. (in preparation)], the Jin et al. (2012) sample of unobscured Seyfert 1 nuclei and quasars, and the Rose et al. (in preparation) sample of nearby AGN selected from the 2MASS sample on the basis of their red near-IR colours. A major advantage of these samples compared to those used in the previous section is that the $[O\text{ III}]$ emission line profiles have been fitted using the same multiple Gaussian fitting technique that we have used for the ULIRGs in this paper. The general properties of these samples are compared with those of the Sy-ULIRGs in Table 10.

We use the velocity shifts and FWHM of the broad and intermediate emission line components as our main indicators of the degree of kinematic disturbance. A complication with this approach is that

Table 7. Mean and the standard error of the mean (σ/\sqrt{N}) for the kinematic parameters measured in the various samples. The entries in the table labelled as ‘all’ correspond to the values considering the four comparison samples together.

Sample	<i>AI20</i>	<i>K1</i>	<i>W20</i> (km s ⁻¹)	<i>W50</i> (km s ⁻¹)
Heckman et al. (1981) <i>N</i> = 36	0.11 ± 0.03	0.88 ± 0.02	798 ± 69	455 ± 40
Whittle (1985) <i>N</i> = 36	0.10 ± 0.02	0.80 ± 0.03	632 ± 40	329 ± 24
Veilleux (1991a) <i>N</i> = 16	0.12 ± 0.06	0.78 ± 0.04	700 ± 122	374 ± 73
Nelson & Whittle (1995) – <i>N</i> = 77		0.87 ± 0.02	682 ± 47	388 ± 28
All samples	0.10 ± 0.01	0.85 ± 0.02	689 ± 41	384 ± 16
This paper <i>N</i> = 17	0.27 ± 0.06	0.74 ± 0.06	1423 ± 131	713 ± 102

Table 8. The results of the 2D KS test of Peacock (1983), comparing our sample of Sy-ULIRGs with the comparison samples. Column 1: sample name. Column 2: 2D statistics. Columns 3 and 4: the two parameter combinations considered for the 2D KS test.

Sample (1)	(2)	<i>AI20</i> versus <i>K1</i> (3)	<i>AI20</i> versus <i>W20</i> (4)
Heckman et al. (1981)	<i>D</i>	0.52	0.56
	<i>P</i> (per cent)	0.6	0.2
Whittle (1985)	<i>D</i>	0.46	0.70
	<i>P</i> (per cent)	2	<0.1
Veilleux (1991a)	<i>D</i>	0.36	0.70
	<i>P</i> (per cent)	22	<0.1
Nelson & Whittle (1995)	<i>D</i>	–	0.62
	<i>P</i> (per cent)	–	<0.1
All	<i>D</i>	0.43	0.66
	<i>P</i> (per cent)	0.6	<0.1

individual objects – including many of the ULIRGs discussed in this paper – may have two or more broad and/or intermediate emission line components. In such cases, we use the flux-weighted mean shift and FWHM of the broad and intermediate emission line components (defined in Section 3.3); this yields single estimates of the shift and FWHM for each object and allows fair comparison of the degree of kinematic disturbance between the various samples. Note that all the velocity shifts and FWHM are measured relative to

Table 9. The results of the 1D two sample KS tests, comparing *AI20*, *K1*, *W50* and *W20* for our sample of Sy-ULIRGs with those of the four comparison samples.

Sample (1)	(2)	<i>AI20</i> (3)	<i>K1</i> (4)	<i>W50</i> (5)	<i>W20</i> (6)
Heckman et al. (1981)	<i>D</i>	0.47	0.43	0.48	0.63
	<i>P</i> (per cent)	0.6	2	0.5	<0.1
Whittle (1985)	<i>D</i>	0.53	0.20	0.62	0.77
	<i>P</i> (per cent)	0.15	65	<0.1	<0.1
Veilleux (1991a)	<i>D</i>	0.33	0.18	0.64	0.75
	<i>P</i> (per cent)	24	93	0.1	<0.1
Nelson & Whittle (1995)	<i>D</i>	–	0.33	0.57	0.66
	<i>P</i> (per cent)	–	7.5	<0.1	<0.1
All	<i>D</i>	0.47	0.27	0.56	0.68
	<i>P</i> (per cent)	0.2	17	<0.1	<0.1

the rest frames of the host galaxies, and narrow emission line components (by our definition FWHM < 500 km s⁻¹) are not included in the analysis.

Fig. 8 shows the velocity shift plotted against the FWHM for the Sy-ULIRGs and the three comparison samples. Again, the figure shows the well-known tendency for the kinematically disturbed components to be blueshifted relative to the host galaxy rest frames. Also, there is a tendency for the objects with the largest blueshifts to have the largest FWHM (see also Spoon & Holt 2009), although the converse is not true, indeed the object with the largest FWHM – the Sy-ULIRG F23389+0300 – shows a slight redshift. Consistent with the results of the previous section, we find that although a significant proportion of the Sy-ULIRGs fall within the main envelope of points defined by the three comparison samples ($\Delta V > -500$ km s⁻¹, FWHM < 1500 km s⁻¹), 50 per cent are outliers on these plots with $\Delta V < -500$ km s⁻¹ and/or FWHM > 1500 km s⁻¹; this proportion is higher than found in the PG quasar (15 per cent), unobscured type I (12 per cent), and 2MASS (34 per cent) samples. We further note that detailed examinations of the spectra of the objects in the high-luminosity comparison samples reveals no objects with the type of highly structured, extremely blueshifted, multiple component [O III] emission profiles that are observed in the Sy-ULIRGs F13451+1232 and F14394+4332.

We again use the Peacock (1983) 2D KS test to investigate the significance of the differences between the positions of the Sy-ULIRGs and the comparison samples in Fig. 8. The results are shown in Table 11. From this it is clear that we can reject the null hypothesis that the Sy-ULIRGs, PG quasars and unobscured type I AGN objects are drawn from the same parent population at the ~ 2 per cent ($\sim 2\sigma$) level of significance, but do not find a

Table 10. Details of the properties of the higher luminosity AGN comparison samples.

Sample	Selection criteria	Redshift range	$L_{[\text{O III}]}$ range (W)	Resolution (km s ⁻¹)	References
Sy-ULIRGs	$S_{60} > 1$ Jy, $L_{\text{IR}} > 10^{12} L_{\odot}$, emission line ratios	$z < 0.175$	$2 \times 10^{33} - 4 \times 10^{35}$	~ 230	This paper
PG quasars	UV excess, broad lines $M_B < -23$	$z < 0.5$	$5 \times 10^{33} - 5 \times 10^{36}$	~ 350	Boroson, Oke & Green (1982)
Unobscured type I	Type 1, X-ray bright unobscured	$z < 0.4$	$2 \times 10^{33} - 3 \times 10^{35}$	~ 160	Jin et al. (2012)
2MASS AGN	$(J - K) > 2$	$z < 0.29$	$3 \times 10^{33} - 6 \times 10^{35}$	~ 550	Rose et al. (in preparation)

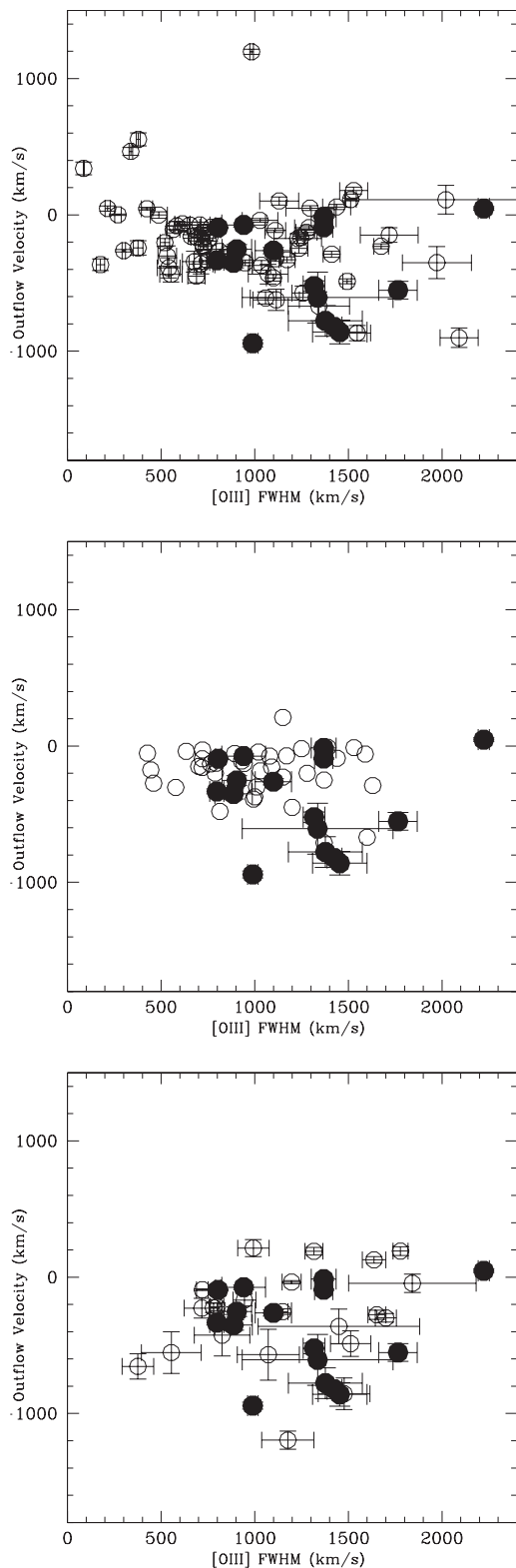


Figure 8. Flux-weighted mean shifts plotted against the flux weighted mean FWHM for the ULIRGs in our sample (black filled circles) and the PG QSOs (top), the Jin et al. (2012) sample of unobscured Seyfert I nuclei and quasars (middle) and the Rose et al. (in preparation) sample of nearby AGN selected from the 2MASS sample on the basis of their red near-IR colours (bottom). The figure shows that the proportion of objects that show extreme emission line kinematics in the sense that they are outliers in the plot is higher for the Sy-ULIRGs than it is from the comparison samples.

Table 11. The results of the 2D KS test of Peacock (1983), comparing our sample of Sy-ULIRGs with the three comparison samples.

Comparison sample	N	2D KS statistic (D)	P (per cent)
PG quasars	85	0.45	1.9
Unobscured type I	30	0.47	2.4
2MASS AGN	30	0.32	38

Table 12. The results of the 1D two sample KS tests, comparing the FWHM and velocity shift distributions for our sample of Sy-ULIRGs with those of the three comparison samples.

Comparison sample	FWHM		Shift	
	D	P (per cent)	D	P (per cent)
PG quasars	0.48	0.3	0.34	7.6
Unobscured type I	0.43	1.9	0.40	4
2MASS AGN	0.28	38	0.24	60

statistically significant difference between the Sy-ULIRGs and the local 2MASS AGN population.

We have also compared the distributions of FWHM and velocity shift separately using a 1D two-sample KS test. The results shown in Table 12 reveal that the most significant differences are between the distributions of FWHM for the Sy-ULIRG and the PG quasars, with the difference significant at the 0.3 per cent ($\sim 3\sigma$) level. This difference is consistent with that found between the line widths of the Sy-ULIRG and non-ULIRG Seyfert comparison samples in the previous section. The differences between the 1D distributions of velocity shift for the Sy-ULIRGs, PG quasars and unobscured Type I samples are less significant and, consistent with the results of the 2D KS test, the 1D tests provide no evidence for significant differences between the FWHM and velocity shifts when comparing the Sy-ULIRGs with the local 2MASS sample.

Together, the results of this section show a tendency for the Sy-ULIRGs to display a higher degree of kinematic disturbance than the PG quasars and unobscured type I AGN, but again observations of larger samples of Sy-ULIRGs will be required to strengthen the statistics.

5 CONCLUSIONS AND FUTURE WORK

Most of the recent investigations of outflows in ULIRGs have focused on observations of the neutral and molecular gas (e.g. Rupke et al. 2005c; Fischer et al. 2010; Rupke & Veilleux 2011; Sturm et al. 2011). These have revealed massive, highly energetic outflows in several objects, supporting the view that the feedback effect associated with the outflows can have a significant impact on the evolution of the host galaxies. However, there remain questions about whether these molecular and neutral outflows are driven by the circumnuclear starbursts or by the AGN that are found in the nuclei of some of the sources. Indeed many such studies have failed to find significant differences between the outflows in ULIRGs with and without powerful AGN (e.g. Rupke et al. 2005c).

Given that (a) we find that a significantly higher fraction of the ULIRGs with optical Seyfert nuclei show evidence for nuclear outflows than those lacking such nuclei, and (b) the outflow components have line ratios consistent with AGN- rather than starburst-photoionization, it is highly likely that the nuclear outflows in the Sy-ULIRGs are indeed driven by the AGN. We also find that the Sy-ULIRGs present outflows that are more extreme than those in samples of local non-ULIRG Seyfert galaxies.

Clearly, there is now evidence that the AGN associated with ULIRGs drive warm outflows. What remains uncertain is whether these outflows are sufficiently energetic and massive to affect the star formation histories and evolution of the host merger remnants. In Section 3.8, we estimated the ranges of mass outflow rates and kinetic powers that are consistent with our observations. At the upper end of the range, the mass outflow rates and kinetic powers of the warm outflows in Sy-ULIRGs are comparable with those typically estimated for the neutral outflows detected using the optical Na I D lines ($6 < \dot{M} < 400 M_{\odot} \text{ yr}^{-1}$; $3 \times 10^{40} < \dot{E} < 10^{44} \text{ erg s}^{-1}$; Rupke et al. 2005b,c; Rupke & Veilleux 2011) and the molecular outflows using the hydroxyl molecule OH (Sturm et al. 2011, up to $1.2 \times 10^3 M_{\odot} \text{ yr}^{-1}$), and would be likely to have a major impact on the host galaxies. On the other hand, if the lower limiting estimates were to prove more typical of the true outflow properties, the warm outflows would be insignificant compared with the neutral and molecular outflows, and therefore unlikely to significantly affect the evolution of the host galaxies.

Despite the high degree of uncertainty, there is cause for optimism that the mass outflow rates and kinetic power estimates will be substantially improved in the near future. In particular, using the transauroral [O II] and [S II] line ratios, it will be possible to make density and reddening estimates that are considerably more precise (see Holt et al. 2011); the outflow radius estimates will benefit from *HST* narrow-band (e.g. Batcheldor et al. 2007) and AO-assisted near-IR imaging; the reddening (and hence H β luminosities) will be further refined by combining optical and near-IR measurements of the hydrogen recombination line fluxes.

ACKNOWLEDGEMENTS

JRZ acknowledges financial support from the Spanish grant AYA2010_21887-C04-04. The William Herschel Telescope is operated on the island of La Palma by the Isaac Newton Group in the Spanish Observatorio del Roque de los Muchachos of the Instituto de Astrofísica de Canarias. MR acknowledges support from STFC and PPARC in the form of PhD studentships. We thank Todd Boroson for providing the reduced spectra of the PG quasar sample. This research is supported in part by STFC grant St/J001589/1.

REFERENCES

Alexander D. M., Bauer F. E., Chapman S. C., Smail I., Blain A. W., Brandt W. N., Ivison R. J., 2005, *ApJ*, 632, 736
 Alexander D. M., Swinbank A. M., Smail I., McDermid R., Nesvadba N. P. H., 2010, in Maraschi L., Ghisellini G., Della Ceca R., Tavecchio F., eds, *ASP Conf. Ser. Vol. 427, Accretion and Ejection in AGN: a Global View*. Astron. Soc. Pac., San Francisco, p. 74
 Allen M. G., Groves B. A., Dopita M. A., Sutherland R. S., Kewley L. J., 2008, *ApJS*, 178, 20
 Armus L., Heckman T., Miley G., 1990, *ApJ*, 364, 471
 Armus L., Heckman T. M., Miley G. K., 1988, *ApJ*, 326, L45
 Armus L. et al., 2007, *ApJ*, 656, 148
 Baldwin J. A., Phillips M. M., Terlevich R., 1981, *PASP*, 93, 5
 Batcheldor D., Tadhunter C., Holt J., Morganti R., O’Dea C. P., Axon D. J., Koekemoer A., 2007, *ApJ*, 661, 70
 Benson A. J., Bower R. G., Frenk C. S., Lacey C. G., Baugh C. M., Cole S., 2003, *ApJ*, 599, 38
 Boroson T. A., Oke J. B., Green R. F., 1982, *ApJ*, 263, 32
 Calzetti D., Armus L., Bohlin R., Kinney A., Koornneef J., Storchi-Bergman T., 2000, *ApJ*, 533, 682
 Cole G., Pedlar A., Holloway A., Mundell C., 1999, *MNRAS*, 310, 1033
 Condon J., Huang Z.-P., Yin Q., Thuan T., 1991a, *ApJ*, 378, 65

Condon J. J., Anderson M. L., Helou G., 1991b, *ApJ*, 376, 95
 Dahari O., De Robertis M. M., 1988, *ApJS*, 67, 249
 De Robertis M. M., Osterbrock D. E., 1986, *ApJ*, 301, 727
 di Matteo T., Springel V., Hernquist L., 2005, *Nat*, 433, 604
 Dicken D., Tadhunter C., Axon D., Robinson A., Morganti R., Kharb P., 2010, *ApJ*, 722, 1333
 Dopita M. A., Sutherland R. S., 1995, *ApJ*, 455, 468
 Dopita M. A., Sutherland R. S., 1996, *ApJS*, 102, 161
 Fabian A. C., 1999, *MNRAS*, 308, L39
 Farrah D., Surace J. A., Veilleux S., Sanders D. B., Vacca W. D., 2005, *ApJ*, 626, 70
 Farrah D. et al., 2007, *ApJ*, 667, 149
 Feruglio C., Maiolino R., Piconcelli E., Menci N., Aussel H., Lamastra A., Fiore F., 2010, *A&A*, 518, L155
 Fischer J. et al., 2010, *A&A*, 518, L41
 Gaskell C. M., Ferland G. J., 1984, *PASP*, 96, 393
 Genzel R. et al., 1998, *ApJ*, 498, 579
 González-Martín O., Masegosa J., Márquez I., Guainazzi M., 2009, *ApJ*, 704, 1570
 Greene J. E. et al., 2010, *ApJ*, 721, 26
 Groves B. A., Dopita M. A., Sutherland R. S., 2004a, *ApJS*, 153, 9
 Groves B. A., Dopita M. A., Sutherland R. S., 2004b, *ApJS*, 153, 75
 Gu Q., Melnick J., Cid Fernandes R., Kunth D., Terlevich E., Terlevich R., 2006, *MNRAS*, 366, 480
 Harrison C. M. et al., 2012, *ApJ*, 760, 15
 Heckman T. M., Miley G. K., van Breugel W. J. M., Butcher H. R., 1981, *ApJ*, 247, 403
 Heckman T., Armus L., Miley G., 1990, *ApJS*, 74, 833
 Hill G. J., Wynn-Williams C. G., Becklin E. E., 1987, *ApJ*, 316, 11
 Holt J., Tadhunter C. N., Morganti R., 2003, *MNRAS*, 342, 227
 Holt J., Tadhunter C., Morganti R., Bellamy M., González Delgado R. M., Tzioumis A., Inskip K. J., 2006, *MNRAS*, 370, 1633
 Holt J., Tadhunter C. N., Morganti R., 2008, *MNRAS*, 387, 639
 Holt J., Tadhunter C. N., Morganti R., 2009, *MNRAS*, 400, 589
 Holt J., Tadhunter C. N., Morganti R., Emonts B. H. C., 2011, *MNRAS*, 410, 1527
 Hopkins P. F., Elvis M., 2010, *MNRAS*, 401, 7
 Hopkins P. F., Hernquist L., Cox T. J., Di Matteo T., Martini P., Robertson B., Springel V., 2005, *ApJ*, 630, 705
 Jin C., Ward M., Done C., Gelbord J., 2012, *MNRAS*, 420, 1825
 Johansson P. H., Burkert A., Naab T., 2009, *ApJ*, 707, L184
 Kauffmann G. et al., 2003, *MNRAS*, 346, 1055
 Kewley L. J., Heisler C. A., Dopita M. A., Lumsden S., 2001, *ApJS*, 132, 37
 Kewley L. J., Groves B., Kauffmann G., Heckman T., 2006, *MNRAS*, 372, 961
 Kim D.-C., Sanders D. B., 1998, *ApJS*, 119, 41
 Kim D. C., Veilleux S., Sanders D. B., 2002, *ApJ*, 143, 277
 Knapen J., Laine S., Yates J. A., Robinson A., Richards A., Doyon R., Nadeau D., 1997, *ApJ*, 490, L29
 LaMassa S. M., Heckman T. M., Ptak A., Hornschemeier A., Martins L., Sonnentrucker P., Tremonti C., 2009, *ApJ*, 705, 568
 LaMassa S. M., Heckman T. M., Ptak A., Martins L., Wild V., Sonnentrucker P., 2010, *ApJ*, 720, 786
 Lípari S., Terlevich R., Díaz R. J., Taniguchi Y., Zheng W., Tsvetanov Z., Carranza G., Dottori H., 2003, *MNRAS*, 340, 289
 Majewski S., Herold M., Koo D., Illingworth G., Heckman T., 1993, *ApJ*, 403, 125
 Markwardt C. B., 2009, in Bohlender D. A., Durand D., Dowler P., eds, *ASP Conf. Ser. Vol. 411, Astronomical Data Analysis Software and Systems XVIII*. Astron. Soc. Pac., San Francisco, p. 251
 Massaro F. et al., 2009, *ApJ*, 692, L123
 Moustakas J., Kennicutt R. C. Jr, 2006, *ApJS*, 164, 81
 Nagar N., Wilson A., Falcke H., Veilleux S., Maiolino R., 2003, *A&A*, 409, 115
 Nelson C. H., Whittle M., 1995, *ApJS*, 99, 67
 Osterbrock D. E., 1989, *Astrophysics of Gaseous Nebulae and Active Galactic Nuclei*. University Science Books, Mill Valley, CA

- Osterbrock D. E., Ferland G. J., 2006, Book Review: Astrophysics of Gaseous Nebulae and Active Galactic Nuclei, 2nd. edn. University Science Books, Sausalito, CA
- Osterbrock D., Fulbright J., Keane M., Trager S., 1996, *PASP*, 108, 277
- Peacock J. A., 1983, *MNRAS*, 202, 615
- Robinson T. G., Tadhunter C. N., Axon D. J., Robinson A., 2000, *MNRAS*, 317, 922
- Rodríguez Zaurín J., Tadhunter C. N., González Delgado R. M., 2009, *MNRAS*, 400, 1139
- Rodríguez Zaurín J., Tadhunter C. N., González Delgado R. M., 2010, *MNRAS*, 403, 1317
- Rupke D. S. N., Veilleux S., 2011, *ApJ*, 729, L27
- Rupke D., Veilleux S., Sanders D., 2005a, *ApJS*, 160, 87
- Rupke D., Veilleux S., Sanders D., 2005b, *ApJS*, 160, 115
- Rupke D., Veilleux S., Sanders D., 2005c, *ApJ*, 632, 751
- Sanders D. B., Mirabel I. F., 1996, *ARA&A*, 34, 749
- Sanders D. B., Soifer B. T., Elias J. H., Madore B. F., Matthews K., Neugebauer G., Scoville N. Z., 1988a, *ApJ*, 325, 74
- Sanders D. B., Soifer B. T., Elias J. H., Neugebauer G., Matthews K., 1988b, *ApJ*, 328, L35
- Scoville N. Z. et al., 2000, *ApJ*, 119, 991
- Silk J., Rees M. J., 1998, *A&A*, 331, L1
- Soto K. T., Martin C. L., 2012, *ApJS*, 203, 3
- Soto K. T., Martin C. L., Prescott M. K. M., Armus L., 2012, *ApJ*, 757, 86
- Spoon H. W. W., Holt J., 2009, *ApJ*, 702, L42
- Spoon H. W. W., Armus L., Marshall J. A., Bernard-Salas J., Farrah D., Charmandaris V., Kent B. R., 2009, *ApJ*, 693, 1223
- Springel V., Di Mateo T., Hernquist L., 2005, *MNRAS*, 361, 776
- Sturm E., González-Alfonso E., Veilleux S., Fischer J., Graciá-Carpio J., Hailey-Dunsheath S., Contursi A., 2011, *ApJ*, 733, L16
- Surace J. A., Sanders D. C., 1999, *ApJ*, 512, 162
- Surace J. A., Sanders D. B., 2000, *AJ*, 120, 604
- Surace J. A., Sanders D. B., Vacca W. D., Veilleux S., Mazzarella J. M., 1998, *ApJ*, 492, 116
- Surace J. A., Sanders D. B., Evans A. S., 2000, *ApJ*, 529, 170
- Taylor M. D., Tadhunter C. N., Robinson T. G., 2003, *MNRAS*, 342, 995
- Thompson T. A., Quataert E., Waxman E., Murray N., Martin C. L., 2006, *ApJ*, 645, 186
- Tremblay G. R. et al., 2009, *ApJS*, 183, 278
- Ulvestad J. S., Wilson A., 1984, *ApJ*, 278, 544
- Veilleux S., 1991a, *ApJS*, 75, 357
- Veilleux S., 1991b, *ApJS*, 75, 383
- Veilleux S., Sanders D., Kim D.-C., 1997, *ApJ*, 484, 92
- Veilleux S., Kim D.-C., Sanders D. B., 1999, *ApJ*, 522, 113
- Veilleux S., Kim D. C., Sanders D. B., 2002, *ApJ*, 143, 315
- Veilleux S. et al., 2009, *ApJS*, 182, 628
- Villar-Martín M., Binette L., Fosbury R. A. E., 1999, *A&A*, 346, 7
- Westmoquette M. S., Clements D. L., Bendo G. J., Khan S. A., 2012, *MNRAS*, 424, 416
- Whittle M., 1985, *MNRAS*, 213, 1
- Whittle M., Pedlar A., Meurs E. J. A., Unger S. W., Axon D. J., Ward M. J., 1988, *ApJ*, 326, 125
- Wilman R. J., Crawford C. S., Abraham R. G., 1999, *MNRAS*, 309, 299
- Yuan T.-T., Kewley L. J., Sanders D. B., 2010, *ApJ*, 709, 884
- Zakamska N. L. et al., 2003, *AJ*, 126, 2125

APPENDIX A: DESCRIPTION OF INDIVIDUAL OBJECTS

F00188–0856. Veilleux, Kim & Sanders (1999) classified this compact object as a LINER at optical wavelengths. However, based on the Kewley et al. (2006, hereafter Kw06) classification scheme, Yuan et al. (2010) classified it as ‘Sy2:’, meaning that *F00188–0856* has an Sy2 spectral type in two of the three BPT diagrams used for its optical classification (see Yuan et al. 2010 for details). Therefore, we included this object in the sample discussed in this paper.

F00188–0856 is one of the two cases (along with *F23327+2913*), for which the [O III] $\lambda\lambda 4959, 5007$ and $H\beta$ emission lines have a low equivalent width, and are potentially affected by noise and residual structure in the underlying continuum. Therefore, these lines are not, in this case, suitable for deriving a model to fit to the other lines in the spectrum. For this object, we used the approach of first fitting the $H\alpha + [N II]$ complex and then modelling the other emission lines in the spectrum with the same components and the same velocity widths and shifts as $H\alpha$. In addition, due to the presence of a telluric absorption feature that coincides with the location of the [S II] $\lambda\lambda 6716, 6731$, it was not possible to model this emission blend.⁷ The results of the $H\alpha + [N II]$ modelling are shown in Fig. 1.

The best-fitting model comprises two components: a narrow component with $\text{FWHM} = 269 \pm 5 \text{ km s}^{-1}$ plus an intermediate component with $\text{FWHM} = 904 \pm 75 \text{ km s}^{-1}$ blueshifted by $-253 \pm 36 \text{ s}^{-1}$ with respect to the narrow component. Using these results, it is possible to measure the line ratios associated with each individual component and then study the corresponding ionization mechanisms using the already mentioned Kw06 classification scheme. We find that the line ratios associated with the narrow component are consistent with a composite spectral type (CP) or LINER, while those corresponding to the intermediate component are consistent with Sy2 ionization, but lie close to the Sy2/LINER limiting region.

F01004–2237. The optical spectrum of this single nucleus system shows a mixture of H II and Sy2 features (Veilleux et al. 1999). However, it was classified as an ‘Sy2:’ in the work of Yuan et al. (2010) and therefore, we included it in our sample.

Fig. 1 shows the [O III] model for this galaxy, which includes three components: an unresolved, narrow component, an intermediate component ($\text{FWHM} = 850 \pm 71 \text{ km s}^{-1}$) blueshifted by $-230 \pm 32 \text{ km s}^{-1}$ with respect to the narrow component and a broad ($\text{FWHM} = 1590 \pm 92 \text{ km s}^{-1}$) component blueshifted by $-999 \pm 80 \text{ km s}^{-1}$ with respect to the narrow component. Note that the broad, shifted components dominate the [O III] emission line flux in this case.

Due to the number of components, the degeneracy between the different models that adequately fit the emission line profiles is a relatively important issue for this object. For example, when the intensities of the different components were left as a free parameter during the modelling of the $H\alpha + [N II]$ complex, the [N II] $\lambda 6583/H\alpha$ line ratio corresponding to the broad component was ~ 4 . As shown in Yuan et al. (2010), their fig. 2, this line ratio is always smaller than ~ 3 . Therefore, during the modelling, we set the value of the [N II] $\lambda 6583/H\alpha$ line ratio to 3, obtaining a good fit to the [N II] + $H\alpha$ blend.

In addition, the [S II] 6716/6731 line ratio was higher than 1.42 (the low-density limit) for the narrow component, but lower than 0.44 (the high-density limit) for the two broad components (i.e. the results were unphysical) when making free fits to the [S II] blend. Therefore, during the modelling, we also forced the values of these line ratios to be 1.42 and 0.44 for the narrow and the two broad components, respectively. Then, the value of one of these line ratios was changed in steps of 0.02 while the values of the other two

⁷ There are cases for which a telluric absorption feature affects the profiles of some lines (mainly [S II] $\lambda\lambda 6716, 6731$ and the $H\alpha + [N II]$ $\lambda\lambda 6548, 6583$ complex) but it is still possible to model the emission lines. However, the flux values derived from the modelling will be relatively unconstrained. An example of the typical effect of a telluric absorption feature on the profile of the $H\alpha + [N II]$ $\lambda\lambda 6548, 6583$ complex is shown in Fig. A6.

remained unchanged until the fit was deemed not adequate. We estimate a lower limit for the intensity ratio [S II] 6716/6731 of 1.2 for the narrow component while acceptable fits are obtained for any line ratio value within the allowed range ($0.44 \leq [\text{S II}] 6716/6731 \leq 1.42$) in the cases of intermediate and the broad components.

Regarding the ionization mechanisms associated with each of the individual components, we find that the line ratios corresponding to the narrow and intermediate components are consistent with H II ionization or fall close to the H II/Sy2 limiting region in the diagrams. On the other hand, the line ratios associated with the broad component are consistent with narrow-line AGN (NLAGN) and Sy2 ionization in two of the BPT diagrams, while they fall close to the H II/Sy2 limiting region in the [S II] diagram. Given these results, it is clear why the spectral classification of this object, based on line ratios derived from integrated line fluxes (e.g. Veilleux et al. 1999), was ambiguous in previous studies; our analysis shows the clear presence of an AGN associated with the broad, blueshifted emission line components. Note that the approach used to model the [S II] 6716/6731 doublet does not significantly change these results.

The nuclear emission line kinematics of this object have been discussed in the past by Armus, Heckman & Miley (1988), Lípári et al. (2003) and Farrah et al. (2005). While the spectra of Armus et al. (1988) and Lípári et al. (2003) show the same blue wings of the [O III] emission lines that we detect in the spectrum presented in this study, Farrah et al. (2005) report that they failed to detect the blue wings in their *HST*/STIS spectrum (0.2 arcsec slit width) that isolates the compact knot in the nucleus of the galaxy. This is interesting because it suggests that the AGN outflow may be significantly extended in this object. However, the substantially worse spectral resolution of the *HST*/STIS spectra of Farrah et al. (2005) compared with the spectra presented in this paper may have prevented the detection of the shifted features.

F12072–0444. As in the case for F00188–0856, the presence of a telluric absorption feature coinciding with the location of the [S II] $\lambda\lambda 6716, 6731$ blend prevents any attempt to model this feature for this Sy2 galaxy. The best-fitting model to all the other observed emission lines comprises three components: a narrow component (FWHM = $275 \pm 8 \text{ km s}^{-1}$) and intermediate component with an FWHM of 525 ± 28 and blueshifted $-276 \pm 30 \text{ km s}^{-1}$ with respect to the narrow component and a broad component with an FWHM of $1343 \pm 81 \text{ km s}^{-1}$ and blueshifted $-446 \pm 35 \text{ km s}^{-1}$. The line ratios measured for all of the three components are consistent with NLAGN or Sy2 ionization.

F13305–1739. F13305–1739 has by far the highest emission line luminosity of all the objects in our sample (see Table 1); its [O III] emission line luminosity would lead to it being classified as a type II quasar according the criteria of Zakamska et al. (2003), and it shows a rich emission line spectrum from the UV ([Mg II] $\lambda 2798$) to the red end ([S II] $\lambda\lambda 6716, 6731$) of its spectrum. Fig. 1 shows the [O III] model that successfully fits all the other emission lines detected in the optical spectrum of this source. Clearly, the broad/shifted components dominate the [O III] emission line flux in this case.

We use the case of F13305–1739 as an example of our modelling technique, and Fig. A1 shows the modelling results obtained for all the emission lines using the so-called [O III] model. This model comprises three components: a narrow component (FWHM = $435 \pm 25 \text{ km s}^{-1}$), a first broad component (B1) with an FWHM of $1276 \pm 29 \text{ km s}^{-1}$ blueshifted by only $-36 \pm 14 \text{ km s}^{-1}$ with respect to the narrow component and a second, broad component (B2) with an FWHM of $1685 \pm 286 \text{ km s}^{-1}$ and blueshifted by $-281 \pm$

29 km s^{-1} with respect to the narrow component. Fig. A1 shows that, in general, the B1 component dominates the flux contribution for the majority of the emission lines detected.

As in the case of F01004–2237, degeneracy is an important issue in the case of F13305–1739. When the intensities of the different components were left as a free parameter during the modelling, the [S II] 6716/6731 line ratio was higher than 1.42 (the low-density limit) for the narrow component, but this ratio was lower than 0.44 (the high-density limit) for the two broad components (i.e. the results were unphysical). Using the same approach described before, we estimate a lower limit for the intensity ratio [S II] 6716/6731 of 1.2 for the narrow, component and an upper limit of 0.6 for the broad components.

In terms of the ionization mechanisms, the line ratios measured for all three kinematic components are consistent with Sy2 ionization. Note that the approach used when modelling the [S II] $\lambda\lambda 6716, 6731$ doublet does not significantly change these result.

F13428+5608 (Mrk 273). This well-known ULIRG is the closest in our sample of Sy-ULIRGs ($z = 0.037$), and in optical images shows an impressive tidal tail that extends over 30 kpc towards the south of the galaxy. A double nucleus structure is visible at near-IR (Armus, Heckman & Miley 1990; Majewski et al. 1993; Knäpen et al. 1997; Scoville et al. 2000) and radio (Ulvestad 1984; Condon et al. 1991a; Cole et al. 1999) wavelengths, with a nuclear separation of ~ 700 pc, although the two nuclei are unresolved in our spectroscopic data.

As shown in Fig. 1, the best-fitting model for this galaxy includes two components: a narrow component with an FWHM of $449 \pm 7 \text{ km s}^{-1}$ plus a broad component with an FWHM of $1369 \pm 62 \text{ km s}^{-1}$ that is redshifted by $14 \pm 12 \text{ km s}^{-1}$ with respect to the narrow component.

We find that, when the intensities of the two components are left as free parameters during the modelling of the H α + [N II] complex, the [N II] $\lambda 6583/\text{H}\alpha$ line ratio measured for the broad component (FWHM = 1369 km s^{-1}) is significantly higher than 3, which, based on the results of Yuan et al. (2010), can be considered as an upper limit for this line ratio. In addition, the [S II] 6716/6731 line ratio obtained for the broad component is outside the allowed range (i.e. [S II] 6716/6731 < 0.44, the high-density limit). Therefore, as discussed before, we set the value of the [N II] $\lambda 6583/\text{H}\alpha$ line ratio to 3 and the [S II] 6716/6731 line ratio at the high-density limit. Then, we gradually increased the value of the [S II] 6716/6731 line ratio until the overall fit was poor, which occurred at the value of 0.8.

In terms of the ionization of the gas, the line ratios measured for the narrow component lie close to the limiting regions between CP and NLAGN ionization, and LINER and Seyfert2 galaxies in the Kwl06 classification scheme. On the other hand, the line ratios measured for the broad component are consistent with Sy2 ionization. Note that the approach used when modelling the H α + [N II] complex and the [S II] $\lambda\lambda 6716, 6731$ doublet does not change this result.

F13451+1232. A detailed discussion of the spectacular emission line kinematics of this object can be found in Holt et al. (2003, 2011).

F14394+5332. F14394+5332 shows the most spectacular [O III] emission line kinematics of all the objects considered in this paper (see Fig. 1), with the clear detection of three distinct narrow components, as well as an underlying broad component. Based on our analysis of the spatially extended [O III] emission line kinematics in this object, the redmost narrow component in the integrated

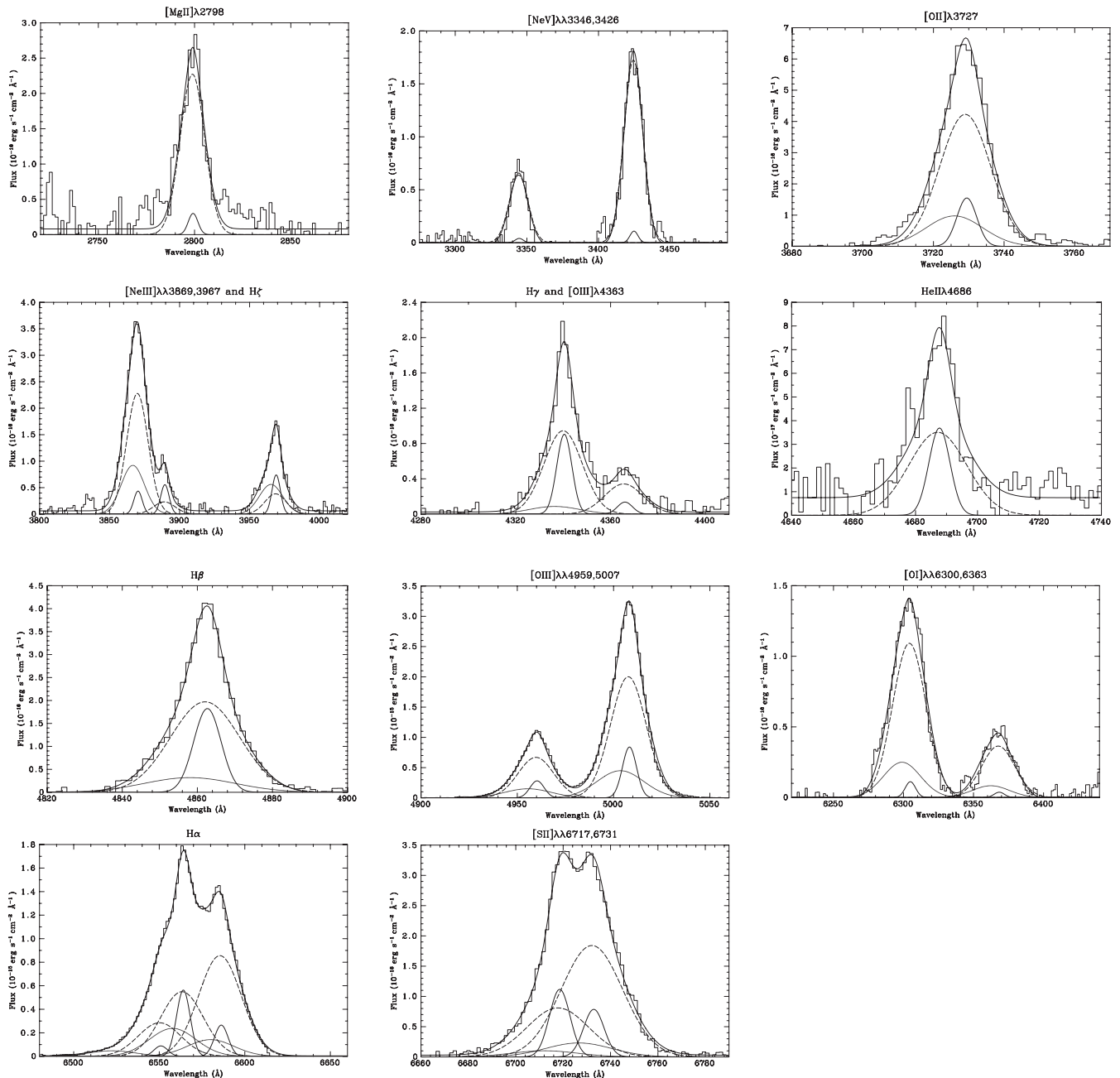


Figure A1. The results obtained by using the [O III] model to fit all the optical emission lines detected in the spectrum of F13305–1739. The resulting model is overlotted (bold line) on the extracted spectrum (faint line). The different kinematic components are also plot in the figure. The solid, dashed and dotted line correspond to the narrow component and the two broad components respectively (referred to as N, B1 and B2 in the text). The figure shows that B1 (dashed line) dominated the flux contribution for the majority of the emission lines detected in the optical spectrum of the source.

spectrum represents the galaxy rest frame. In this case, the two other narrow components are blueshifted by -700 and -1360 km s^{-1} relative to the rest frame, and the underlying broad components are also blueshifted; clearly, this is a case in which the components that are broad and/or blueshifted dominate the [O III] emission line flux. The multicomponent nature of the [O III] lines in this object was also detected by Lípari et al. (2003), albeit at lower S/N.

The profiles of the [O III] emission lines in this object are strikingly different from those of most of the other emission lines. This is illustrated by the comparison between the H β , [O III] and [N I] emission lines shown in Fig. A2. In particular, we do not clearly detect

the blueshifted narrow lines in *any* of the lower ionization lines such as [O II] $\lambda 3727$, H β , [N I] $\lambda 5200$, [O I] $\lambda\lambda 6300, 6363$,⁸ H α , [N II] $\lambda\lambda 6548, 6584$ and [S II] $\lambda\lambda 6717, 6731$, apart from possible hints of the first shifted narrow component in the form of a ‘shelf’ in the blue wings of [N I] $\lambda 5200$ and [O I] $\lambda 6300$. On the other hand, the [Ne III] $\lambda 3869$ line has a profile that is consistent with that of [O III] $\lambda 5007$, although the lower S/N, lower effective velocity resolution

⁸N.B. The blue wing of the [O I] $\lambda 6300$ line may be significantly affected by telluric atmospheric B-band absorption.

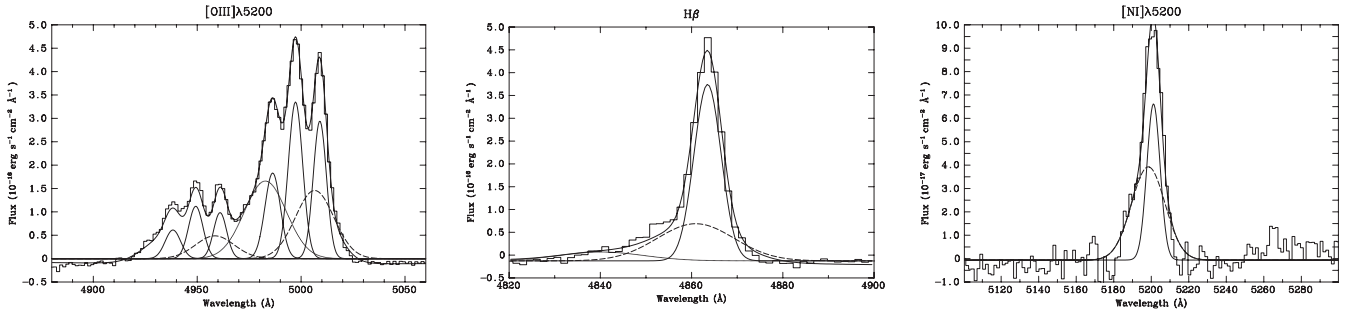


Figure A2. The modelling results obtained for [O III], H β and [N I] λ 5200. The resulting model is overplotted (bold line) on the extracted spectrum (faint line). The different components are also plotted in the figure. The solid, dashed and dotted line correspond to the narrow components (three in the case of the [O III] emission line referred to as N1, N2 and N3 in Table 2) and the two broad components, respectively (referred to as B1 and B2 in Table 2). The figure shows that the blueshifted narrow lines (N2 and N3) are not clearly detected in the lower ionization lines such as H β or [N I] λ 5200.

and possible residual features from the subtraction of the (complex) underlying stellar continuum preclude an accurate comparison between the line profiles. We further note that the [Ne V] λ 3425 and He II (4686) features show evidence for broad, blueshifted features, but the S/N is again too low to allow a detailed comparison with the [O III] line profile.

The fact that the discrete blueshifted [O III] emission lines components are not clearly detected in the other lines, many of which have similar *total* emission line fluxes, immediately implies that the gas emitting these blueshifted narrow components has a high-ionization state. Nonetheless, the low-ionization lines do show some evidence for kinematic disturbance in the form of blue wings. Overall, we find that we can obtain an acceptable fit to all the low-ionization and Balmer lines in the nuclear spectrum using a model that includes a narrow component with the same kinematic properties as those of the redmost (rest-frame) narrow component detected in the [O III] line, plus two broad components blueshifted by -156 and -1574 km s $^{-1}$ with an FWHM of 1272 and 1401 km s $^{-1}$, respectively. We also find that we can fit the [O III] profiles with the same two broad components plus the three narrow components described above; this fit is shown in Fig. 1, and all the corresponding fit components are listed in Table 2.

To get some idea of the ionization of the kinematically disturbed emission line components, we have compared the sum of the fluxes of all the blueshifted components of [O III] (two narrow + two broad) with the sum of the fluxes of the blueshifted components fitted to the lower ionization lines (two broad). The resulting line ratios are labelled ‘B’ in Table 3. Interestingly, despite the fact that the discrete blueshifted narrow components in [O III] must be emitted by gas with a very high ionization state, the overall B line ratios are low ionization in character, with [O II]/[O III] ~ 1 and [O III]/H $\alpha \sim 1$, although more consistent with AGN than starburst heating.⁹ On the other hand, the line ratios for the red narrow component fall squarely in the H II/AGN region of all three diagnostic diagrams.

Clearly, the extraordinary kinematical and ionization properties of this source warrant further investigation with higher resolution and S/N optical spectroscopy.

F15130–1958. Three components were required to adequately model the profile of the emission lines detected in the optical spectrum of this single nucleus ULIRG: a first, intermediate component

(I1, FWHM = 545 ± 69 km s $^{-1}$), a second, intermediate component (I2, FWHM = 700 ± 188 km s $^{-1}$) blueshifted by -351 ± 280 km s $^{-1}$ with respect to I1, and a broad (FWHM = 1630 ± 41 km s $^{-1}$) component blueshifted by -725 ± 131 km s $^{-1}$ with respect to the narrowest component.

As in previous cases, when only the shifts between the different components and their widths are fixed during the modelling of the H α + [N II] complex, the results obtained lead to unphysical H α /H β , [N II] λ 6583/H α line ratio values for I2, and [S II] 6716/6731 line ratios for I2 and the broad component. Therefore, during the modelling, the H β flux of the I2 component was set such that the H α /H β line ratio associated with this component is equal to or higher than that of I1 (H α /H β = 3.74 and 4.01 for I1 and I2 for the best-fitting model). In addition, the [N II] λ 6583/H α line ratio was set to 3 and the [S II] 6716/6731 line ratio was set to 1.42, 0.44 and 0.44 for I1, I2 and the broad component, respectively. The values of each of the [S II] 6716/6731 line ratios was then changed in steps of 0.02, while the values of the other two remained unchanged, until the fit was deemed poor. Hence, we estimate a lower limit for the intensity ratio [S II] 6716/6731 of 1.2 for I1, while acceptable fits are obtained for any line ratio value within the allowed range ($0.44 \leq$ [S II] 6716/6731 ≤ 1.42) in the cases of I2 and the broad component.

Finally, we note that the line ratios of I1 are consistent with NLAGN ionization or fall close to the LINER/Sy2 limiting region in the optical diagrams, whereas the values measured for the I2 and broad components are consistent with Sy2 ionization.

F15462–0450. This is the only Seyfert 1 galaxy included in the sample discussed in this paper. Fig. 1 shows the best-fitting model obtained from fitting simultaneously the H β , [O III] $\lambda\lambda$ 4959, 5007 and the broad Fe II $\lambda\lambda$ 4924, 5018¹⁰ emission lines, typical of Sy1 galaxies. Due to the large number of emission lines close together in wavelength and bearing in mind that multiple (and broad) kinematic components contribute to each individual emission line, clearly overcoming the degeneracy issue is not easy in the case of F15462–0450.

Overall, we find that, with the exception of H β , the Balmer lines (H δ , H γ and H α), are adequately fitted using three kinematic components: a narrow component of width 147 ± 47 km s $^{-1}$ at rest frame, plus a first broad component of width 1509 ± 47 km s $^{-1}$ redshifted by 169 ± 8 km s $^{-1}$ with respect to the narrow component and a second broader component of width 3673 ± 137 km s $^{-1}$

⁹ Note that integrated H β flux for the kinematically disturbed components is likely to be strongly affected by the underlying H β absorption. Therefore, B ratios measured relative to H β are unlikely to be reliable

¹⁰ Note that, in order to model the broad Fe II lines, we assumed that they have the same profile as the broad H β line.

redshifted by 292 ± 21 with respect to the narrow component. In the case of $H\beta$ a fourth, broad component is also required to obtain an adequate fit (see text below for details).

On the other hand, the forbidden lines ($[\text{Ne v}] \lambda\lambda 3346, 3425$, $[\text{O II}] \lambda\lambda 3726, 3728$, $[\text{Ne III}] \lambda\lambda 3868, 3968$, $[\text{O III}] \lambda\lambda 4959, 5007$, $[\text{N II}] \lambda\lambda 6548, 6583$ and $[\text{S II}] \lambda\lambda 6716, 6731$) are adequately fitted using two kinematic components that correspond to those presented in Table 2, and labelled as the $[\text{O III}]$ model for this galaxy: a narrow component at rest frame, consistent with that found for the Balmer lines (i.e. $\text{FWHM} = 147 \pm 47 \text{ km s}^{-1}$ and referred to as ‘N’ in Table 2) plus a broad component ($\text{FWHM} = 1426 \pm 47 \text{ km s}^{-1}$) blueshifted by $-822 \pm 25 \text{ km s}^{-1}$ with respect to the narrow component (referred to as ‘B’ in Table 2). Note that the broad component dominates the $[\text{O III}]$ emission line flux in this object.

The broad component associated with the forbidden lines (B) it is also required to adequately model the profile of the $H\beta$ emission line. Such component is represented by the most redshifted, dashed line Gaussian in the $H\beta$ fit in Fig. 1. Most likely, this component is also present in the other Balmer lines. However, the dominant flux contribution associated with the emission from the BLR as well as the relatively low S/N in the cases of the $H\delta$, $H\gamma$ emission lines prevent a clear detection of this kinematic component for the other Balmer lines. In addition, due to the dominant BLR emission, it is not possible to constrain the flux contribution of the broad component to the $[\text{N II}] \lambda\lambda 6548, 6583$ emission lines with any accuracy.

Given the fact that the broad component present in the forbidden lines is not clearly detected in the $H\alpha$ emission line, no attempt to study the ionization mechanisms was made for that component. Interestingly, the line ratios measured for the narrow component detected in *all* lines are consistent with H II ionization.

F16156+0146. For the study presented here, we used the 5 kpc-I aperture described in the work of Rodríguez Zaurín et al. (2009). This aperture samples the north-western nucleus of this double nucleus system, which is associated with the AGN activity. This is one of the four objects in our sample (along with F13451+1232, F14394+5332 and F23389+0300) for which it is not possible to find one model that fits all the emission lines observed in the optical spectrum. However, it is possible to model all the emission lines using two different approaches: one in which a different model is used to fit each of the detected emission lines and another in which we use two models. In the latter case, the first of the two models adequately fit the $[\text{O III}] \lambda\lambda 4959, 5007$ emission lines, while the second model provides a good fit to all of the other lines.

The best-fitting model for $[\text{O III}] \lambda\lambda 4959, 5007$, which is the same for the two approaches, as shown in Fig. 1 and comprises three components: an unresolved narrow component, an intermediate component ($\text{FWHM} = 804 \pm 20 \text{ km s}^{-1}$) blueshifted by $-186 \pm 10 \text{ km s}^{-1}$ with respect to the narrow component and a broad component ($\text{FWHM} = 1535 \pm 59 \text{ km s}^{-1}$) blueshifted by $-374 \pm 26 \text{ km s}^{-1}$ with respect to the narrow component. The second model, shown in Fig. A3 for the $H\beta$ line comprises another three components: an unresolved component, a narrow component ($\text{FWHM} = 446 \pm 86 \text{ km s}^{-1}$) redshifted by $33 \pm 29 \text{ km s}^{-1}$ with respect to the unresolved component, and a third, broad component ($\text{FWHM} = 1225 \pm 108 \text{ km s}^{-1}$) that is blueshifted by $-150 \pm 48 \text{ km s}^{-1}$ relative to the narrow, unresolved component.

Overall, the fact that we do not find one adequate model for all emission lines suggest that, instead of a discrete number of kinematic components, there may be a continuous range of density, ion-

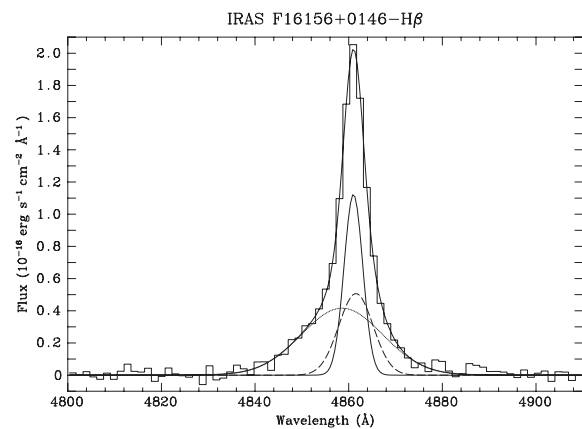


Figure A3. In the case of F16156+0146, it was not possible to model *all* the emission lines using a single model. However, with the exception of the $[\text{O III}] \lambda\lambda 4959, 5007$, it was possible to model the rest of the observed emission lines with the model shown in the figure. This model comprises an unresolved component at rest frame (solid line), a narrow component ($\text{FWHM} = 446 \pm 86 \text{ km s}^{-1}$) redshifted by $33 \pm 29 \text{ km s}^{-1}$ with respect to the unresolved component (dashed line) and a third, broad component ($\text{FWHM} = 1225 \pm 108 \text{ km s}^{-1}$) that is blueshifted by $-150 \pm 48 \text{ km s}^{-1}$ relative to the narrow, unresolved component (dotted line). The resulting model (bold line) is overplotted on the extracted spectrum.

ization and kinematics through the NLR, leading to each line having a different profile. We did not attempt to estimate line ratios associated with the different components in the case of F16156+0146.

F17044+6720. This object was originally classified as a LINER by Veilleux et al. (1999). However, the optical spectroscopic classification of this source was recently reviewed by Yuan et al. (2010), who found that the line ratios of F17044+6720 are typical of an Sy2 galaxy.

Fig. 1 shows the $[\text{O III}] \lambda\lambda 4959, 5007$ model for this galaxy comprising two components: a narrow component of width $\text{FWHM} = 290 \pm 5 \text{ km s}^{-1}$ plus a broad component of width $\text{FWHM} = 1765 \pm 100 \text{ km s}^{-1}$ that is blueshifted by $-553 \pm 65 \text{ km s}^{-1}$ with respect to the narrow component. Due to the presence of a telluric absorption feature it was not possible to model the $[\text{S II}] \lambda\lambda 6716, 6731$ emission lines for this galaxy. The line ratio values measured for the narrow component are consistent with CP ionization, or lie close to the limiting region between LINER and Sy2, while the line ratios associated with the broad component are consistent with NLAGN, or fall close to the LINER/Sy2 ionization.

F17179+5444. Three components are required to model the optical spectrum of this single nucleus Sy2 galaxy. Fig. 1 shows an $[\text{O III}]$ model including a narrow component with an FWHM of $356 \pm 22 \text{ km s}^{-1}$, an intermediate component with an FWHM of $515 \pm 51 \text{ km s}^{-1}$ that is redshifted by $246 \pm 67 \text{ km s}^{-1}$ with respect to the narrow component and a third, broad component with an FWHM of $1562 \pm 41 \text{ km s}^{-1}$ that is blueshifted with respect to the narrow component by $-119 \pm 61 \text{ km s}^{-1}$. The line ratios measured for the narrow component are consistent with CP or LINER ionization, while the line ratios of the shifted components are, in general, consistent with Sy2 ionization.

However, for this galaxy, it is important to add a caveat about the uniqueness of the best-fitting model. As described above, there are two close narrow components that have relatively similar widths (356 ± 22 and $515 \pm 51 \text{ km s}^{-1}$). Therefore, it is possible that this narrow line splitting represents unresolved rotation, or traces a

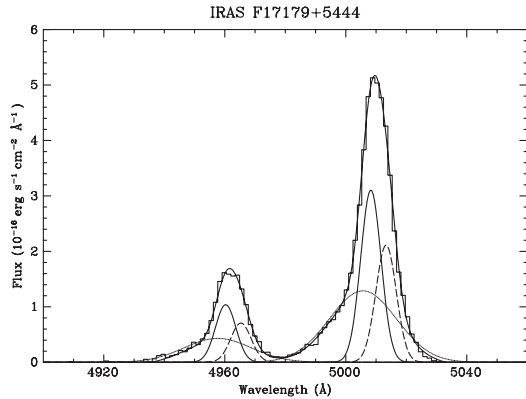


Figure A4. A second, possible [O III] model that adequately fits all the observed emission lines in the case of F17179+5444. The different components shown in figure are a narrow component (N1, $\text{FWHM} = 386 \pm 14 \text{ km s}^{-1}$), a second narrow component (N2) with the same width redshifted by $301 \pm 21 \text{ km s}^{-1}$ with respect to N1 and a broad component ($\text{FWHM} = 1543 \pm 34 \text{ km s}^{-1}$) blueshifted by $-157 \pm 33 \text{ km s}^{-1}$ with respect to N1. This model is interpreted as unresolved rotation

large-scale bipolar outflow in the gas (see for example Holt et al. 2008). To test this scenario, we set the widths of the two narrow components to have the same value during the modelling of the [O III] $\lambda\lambda 4959, 5007$ emission lines; the result is presented in Fig. A4. The model, that also successfully fits all the observed emission lines, comprises three components: a narrow component (N1, $\text{FWHM} = 386 \pm 14 \text{ km s}^{-1}$), a second narrow component (N2) with the same width redshifted by $301 \pm 21 \text{ km s}^{-1}$ with respect to N1 and a broad component ($\text{FWHM} = 1543 \pm 34 \text{ km s}^{-1}$) blueshifted by $-157 \pm 33 \text{ km s}^{-1}$ with respect to N1.

Note that when only the widths and shifts of the different components were constrained for the two best-fitting models described before, the $\text{H}\alpha/\text{H}\beta$ line ratios associated with the intermediate and the N2 component were lower than 2.88, the theoretical lower limit assuming case B recombination theory in absence of reddening. A similar issue is found for the broad component in the case of the [S II] $\lambda\lambda 6716, 6731$ doublet, where the [S II] 6716/6731 line ratio is found to be higher than 1.42, the low-density limit. This is due to the fact that the flux contribution in the case of the [S II] $\lambda\lambda 6716, 6731$ emission lines is dominated by the narrow components at rest frame (for the two best-fitting models considered). Therefore, the intensities of the broad components are relatively unconstrained.

To overcome these problems the $\text{H}\beta$ flux contribution of the intermediate and the N2 was forced to have an intensity such as the $\text{H}\alpha/\text{H}\beta$ line ratio associated with this component is higher or equal to that of the narrow component at rest frame. In addition, following the approach used for other objects, the [S II] 6716/6731 line ratios of the shifted components were set to 0.44 during the modelling and then slightly increased in steps of 0.02 until the fit became poor. As we mentioned before, the flux contribution of these components is relatively small, and adequate fits are obtained for any value of this ratio within the allowed range ($0.44 \geq [\text{S II}] 6716/6731 \geq 1.42$).

In terms of line ratios, we find similar results for the two models described above. The values measured for the narrow component are consistent with CP and LINER ionization. On the other hand, the line ratios of the I and B components are consistent with Sy2 ionization. We note that telluric atmospheric absorption features affect, to some extent, the profile of the [O I] $\lambda 6300$ emission line and the blue wing of the [S II] $\lambda\lambda 6716, 6731$ doublet. Therefore, the

line ratios for the broad components of the latter lines are relatively unconstrained for either of the models considered here.

F23060+0505. Strong emission lines are observed from the UV end (Mg II $\lambda 2798$) to the red end ([S II] $\lambda\lambda 6716, 6731$) of the spectrum of this compact galaxy. The best-fitting model presented in Fig. 1 comprises four components: a narrow (N1, $\text{FWHM} = 376 \pm 6 \text{ km s}^{-1}$), a second, unresolved, narrow component (N2) redshifted by $306 \pm 4 \text{ km s}^{-1}$ with respect to the narrow component at rest frame, a broad component ($\text{FWHM} = 1001 \pm 23 \text{ km s}^{-1}$) blueshifted by $-310 \pm 14 \text{ km s}^{-1}$ with respect to the narrow component at rest frame and a very broad component ($\text{FWHM} = 2148 \pm 125 \text{ km s}^{-1}$) that is blueshifted by $-1073 \pm 122 \text{ km s}^{-1}$ with respect to the narrow component in the rest frame. As in the previous case, it is possible that the observed narrow-line splitting represents unresolved rotation, or traces a large-scale bipolar outflow in the gas.

The very broad component is only detected in high-ionization emission lines ([O III] $\lambda\lambda 4959, 5007$, He II $\lambda 4686$ and [Ne V] $\lambda 3426$). The other observed emission lines, with the exception of $\text{H}\beta$ and the $\text{H}\alpha + [\text{N II}] \lambda\lambda 6549, 6583$ complex, are adequately modelled using a model including the two narrow components plus the broad component. In the case of the $\text{H}\beta$ line and the $\text{H}\alpha + [\text{N II}]$ complex profiles, the blue and red wings are not adequately fitted with a model comprising the two narrow plus a broad component (see Fig. A5). Accounting for a fourth, blueshifted component does not improve the quality of the fit. In fact, when a fourth, broad component consistent with that detected in [O III] is included during the modelling, DIPSO returns negative flux values for this component. Therefore, we used the approach of including a fourth, unconstrained component (i.e. shift, width and flux of this component are free parameters) during the modelling of the $\text{H}\beta$ and $\text{H}\alpha + [\text{N II}]$ emission lines, and the results are shown in Fig. A5. This fourth component has an FWHM of $2345 \pm 368 \text{ km s}^{-1}$ and is redshifted by $188 \pm 100 \text{ km s}^{-1}$ with respect to the narrow component at rest frame; its $\text{H}\alpha/\text{H}\beta$ ratio of 18 ± 2.7 implies a reddening of $E(B - V) = 1.68 \pm 0.14$ assuming a Calzetti et al. (2000) extinction law. At the same time, the nuclear spectrum of the object shows an unusually red continuum compared with other local ULIRGs (Rodríguez Zaurín et al. 2009, see also Hill et al. 1987). Overall, the properties of the nuclear spectrum of this source are consistent with it containing a moderately reddened Seyfert I nucleus. This is consistent with the clear detection at near-IR wavelengths by Veilleux, Sanders & Kim (1997) of a broad Pa α line of similar width ($\text{FWHM} \sim 1954 \text{ km s}^{-1}$) to the broad Balmer lines detected in our optical spectrum.

Note that a telluric absorption feature might affect the blue wing of the $\text{H}\alpha + [\text{N II}]$ complex, as shown in Fig. A6. Nonetheless, we have successfully fitted the $\text{H}\alpha + [\text{N II}]$ blend using a BLR component that has the same width and shift as that fitted to the $\text{H}\beta$ line.

Regarding the ionization mechanisms, we find that the line ratios measured for the three components observed in all the emission lines are consistent with Sy2 ionization. As in some previous cases, when only the shifts between the different components and their widths are fixed, the [S II] 6716/6731 line ratio associated with N2 was higher than 1.42 (the low-density limit), while this value was lower than 0.44 (the high-density limit) for the broad component. Following the approach described before, we set the values of this line ratio to be 0.44 and then change the value for each component individually in steps of 0.02 until the fit was deemed not adequate. Acceptable fits are obtained for any line ratio value within the allowed range ($0.44 \leq [\text{S II}] 6716/6731 \leq 1.42$). Finally, we note that the degeneracy issue associated with the [S II] $\lambda\lambda 6716, 6731$ doublet does not change the

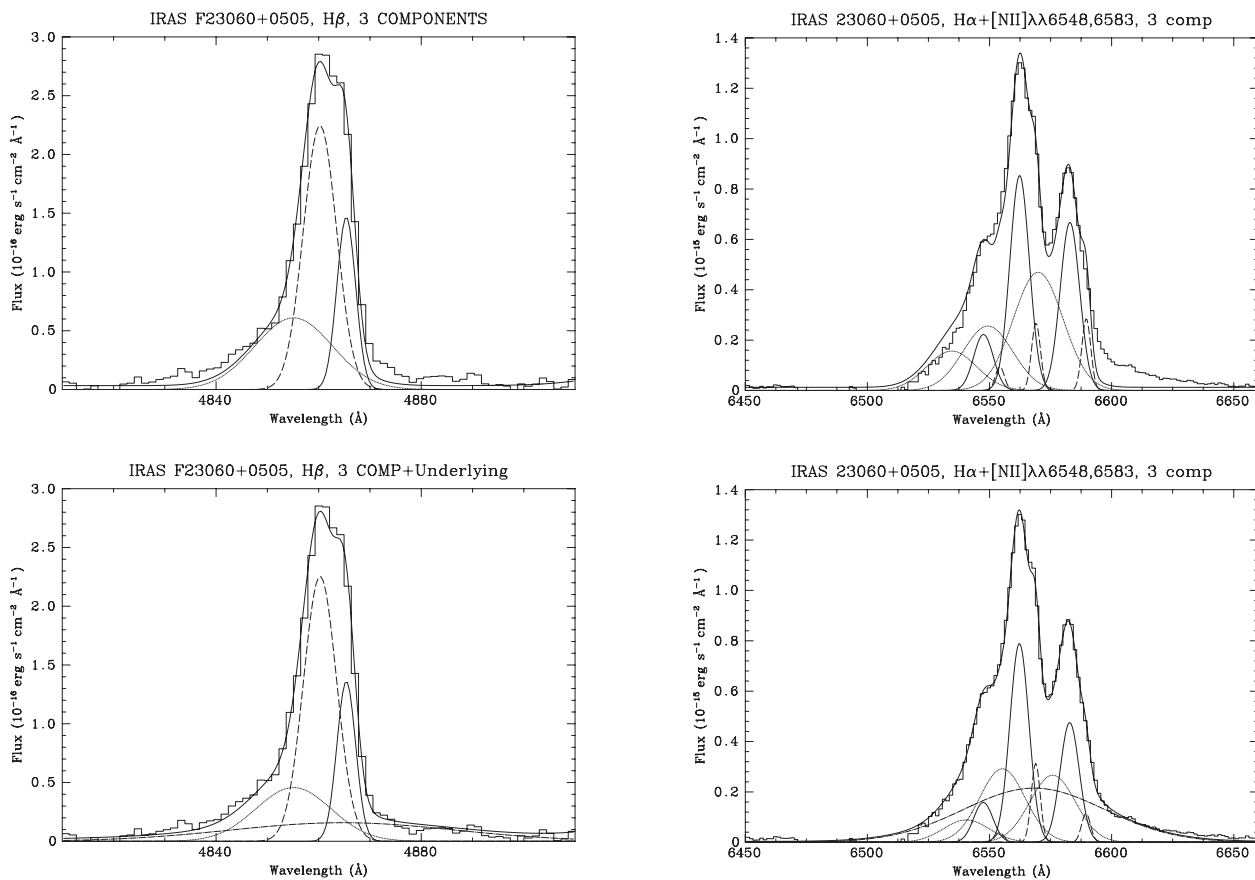


Figure A5. Fits to the optical emission lines in F23060+0505. Top panel: $H\beta$ and $H\alpha + [NII] \lambda\lambda 6549, 6583$ fit including the two narrow components (N1 and N2) plus the broad components corresponding to the $[OIII]$ model for this galaxy. Lower panel: $H\beta$ fit including the already mentioned three components plus an underlying broad component (representing the BLR). When only three components are included in the modelling, the blue, and particularly the red wings of the line profiles are not adequately fitted. The problem disappears when including the underlying broad component.

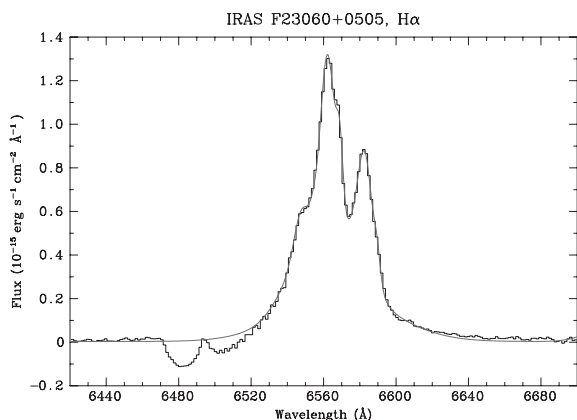


Figure A6. Using the $H\alpha + [NII]$ complex to illustrate the effects of the telluric absorption feature in the case of F23060+0505. Although the telluric feature affects the shape of the profile for the complex, it is still possible to model the $H\alpha$ and the $[NII] \lambda\lambda 6549, 6583$ emission lines using the $[OIII]$ model. The red, solid line is our best-fitting model.

results related to the ionization mechanism, i.e. Sy2-like line ratios are always found for all the different components.

F23233+2817. The $[OIII]$ model for this very compact object comprises four components: a narrow component ($FWHM = 179 \pm$

4 km s^{-1}), an intermediate component ($FWHM = 640 \pm 24 \text{ km s}^{-1}$) blueshifted by $-161 \pm 15 \text{ km s}^{-1}$ with respect to the narrow component, a broad component ($FWHM = 1511 \pm 118$) blueshifted by $-447 \pm 41 \text{ km s}^{-1}$ with respect to the narrow component and a very broad component ($FWHM = 2706 \pm 422 \text{ km s}^{-1}$) that is blueshifted by $-3433 \pm 904 \text{ km s}^{-1}$ with respect to the narrow component. As shown in Fig. 1, the flux contribution of the very broad component is relatively small. Therefore, the uncertainties associated with the corresponding shift and width are large. As in the previous object, this component is only required to obtain an adequate fit in the case of the $[OIII] \lambda\lambda 4959, 5007$. All the other observed lines can be modelled with the first three components listed before.

As in most of the cases, when only the shifts between the different components and their widths are fixed, the $[SII] 6716/6731$ line ratios associated with the intermediate and broad components are outside the allowed range. Therefore, following the approach described above we set the ratio to 0.44 for the intermediate and broad components, and then increase the value of each of these two components in steps of 0.02 until the fit was considered poor. In this way, we estimate an upper limit for the $[SII] 6716/6731$ ratio of 1.0 for these two components.

Regarding the ionizing mechanisms, we find that the line ratios measured for the narrow component are consistent with NLAGN ionization, or fall close to the $HII/Sy2$ limiting region in the diagrams. On the other hand, the line ratios measured for both the

intermediate and the broad components are consistent with Sy2 ionization. Note that that an Sy2 spectral type is found for these two components independently of the [S II] 6716/6731 line ratio used during the modelling.

F23327+2913. Yuan et al. (2010) recently classified this double nucleus system as Sy2:, although it was originally classified as LINER by Veilleux et al. (1999). For the work presented here, we concentrate on the 5 kpc-I aperture described in Rodríguez Zaurín et al. (2009). This aperture covers the emission from the southern source, and is the only aperture for which the corresponding extracted spectrum shows evidence for outflows.

The main problem when trying to model the emission lines in this object is that the [O III] $\lambda\lambda 4959, 5007$ and $H\beta$ emission lines have low equivalent widths, and are potentially affected by noise and residual structure in the underlying continuum. Therefore, these lines are not suitable for deriving a model to fit to the other lines in the spectrum. As in the case of F00188–0856, we use the approach of first fitting the $H\alpha + [N II]$ complex and then model the other emission lines observed in the spectrum with the same components and the same velocity widths and shifts as $H\alpha$. The results of the $H\alpha + [N II]$ modelling are shown in Fig. 1.

The best-fitting model comprises two components: a narrow component ($\text{FWHM} = 109 \pm 2 \text{ km s}^{-1}$) and an intermediate component ($\text{FWHM} = 805 \pm 13 \text{ km s}^{-1}$) blueshifted by $-92 \pm 4 \text{ km s}^{-1}$ with respect to the narrow component. The narrow component makes a negligible contribution to the flux of the $H\beta$ emission line. In fact, the $H\beta$ emission line can be modelled using only the intermediate component. Therefore, it is not possible to study the ionization mechanism associated with that component. Regarding the inter-

mediate component, we find that the line ratios measured for that component are consistent with NLAGN or $H II$ ionization.

F23389+0300. Two 5 kpc apertures (5 kpc-I and 5 kpc-II) were used during the investigation of the stellar populations of this double-nucleus system presented in Rodríguez Zaurín et al. (2009, 2010) However, aperture used for this study is the 5 kpc-I aperture, centred on the northern source, which includes the AGN nucleus (e.g. Nagar et al. 2003).

The [O I] $\lambda\lambda 6300, 6393$ emission lines, which are stronger and more powerful than the observed [O III] $\lambda\lambda 4959, 5007$ emission lines, are particularly impressive in this source. In terms of the modelling, it was not possible to find one model that adequately fits all the detected emission lines. In this particular case, each emission line was fitted using an individual model. For completeness, Fig. 1 shows the modelling result for the [O III] emission lines. The model shown in the figure comprises a narrow component ($\text{FWHM} = 289 \pm 7 \text{ km s}^{-1}$) plus a very broad component ($\text{FWHM} = 2223 \pm 30 \text{ km s}^{-1}$) that is redshifted by $47 \pm 13 \text{ km s}^{-1}$ with respect to the narrow component.

As in the cases of F13451+1232, F14394+5332 and F16156+0146, the fact that we do not find one adequate model for all emission lines suggest that, instead of a discrete number of kinematic components, there may be a continuous range of density, ionization and kinematics through the NLR, leading to each line having a different profile. No attempt has been made to estimate line ratios of the different kinematic components for this galaxy.

This paper has been typeset from a $\text{T}_{\text{E}}\text{X}/\text{L}_{\text{A}}\text{T}_{\text{E}}\text{X}$ file prepared by the author.